



## Source-Dependent Optical and Mineral Signatures of Dust Outbreaks over the Mediterranean

Alkistis Papetta<sup>1</sup>, Celia Herrero del Barrio<sup>2,3</sup>, S. Yeşer Aslanoğlu<sup>3</sup>, Rizos-Theodoros Chadoulis<sup>4,7</sup>, Georgia Charalampous<sup>5,6</sup>, Sara Herrero-Anta<sup>2,3</sup>, Dimitra Kouklaki<sup>7,8</sup>, Michail Mytilinaios<sup>9</sup>, Anna Moustaka<sup>4,10</sup>, Emmanouil Proestakis<sup>7,13</sup>, Vassilis Amiridis<sup>7</sup>, Christos Spyrou<sup>12</sup>, Antonis Gkikas<sup>12</sup>, Michael Pikridas<sup>1</sup>, Maria Kezoudi<sup>1</sup>, Franco Marengo<sup>1</sup>, Jean Sciare<sup>1</sup>, Sophie Vandebussche<sup>11</sup>, Stavros Solomos<sup>12</sup>, Stelios Kazadzis<sup>10</sup>, and Ilias Fountoulakis<sup>12</sup>

<sup>1</sup>Climate and Atmosphere Research Centre (CARE-C), The Cyprus Institute, Nicosia, Cyprus

<sup>2</sup>Group of Atmospheric Optics (GOA-UVa), Universidad de Valladolid, Valladolid, Spain

<sup>3</sup>Laboratory of Disruptive Interdisciplinary Science (LaDIS), Universidad de Valladolid, Valladolid, Spain

<sup>4</sup>Laboratory of Atmospheric Physics, Aristotle University of Thessaloniki, 54124, Greece

<sup>5</sup>Eratosthenes Centre of Excellence, Limassol, Cyprus

<sup>6</sup>Department of Civil Engineering & Geomatics, Cyprus University of Technology, Limassol, Cyprus

<sup>7</sup>Institute for Astronomy, Astrophysics, Space Applications and Remote Sensing, National Observatory of Athens (IAASARS/NOA), 15236 Athens, Greece

<sup>8</sup>Department of Geology and Geoenvironment, National and Kapodistrian University of Athens, Greece

<sup>9</sup>Consiglio Nazionale delle Ricerche - Istituto di Metodologie per l'Analisi Ambientale (CNR-IMAA), Tito, Italy

<sup>10</sup>Physicalisch Meteorologisches Observatorium, World Radiation Center, Davos, Switzerland

<sup>11</sup>Royal Belgian Institute for Space Aeronomy (BIRA-IASB), Brussels, Belgium

<sup>12</sup>Research Centre for Atmospheric Physics and Climatology of the Academy of Athens, Greece

<sup>13</sup>School of Chemical and Environmental Engineering, Technical University of Crete, Chania, Greece

**Correspondence:** Alkistis Papetta (a.papetta@cyi.ac.cy) and Celia Herrero del Barrio (celia@goa.uva.es)

**Abstract.** Dust events frequently affect the Mediterranean Basin, however, the evolution of their optical and microphysical properties during transport remains poorly characterized. This study examines four major dust outbreaks in 2021–2022 affecting the Mediterranean, originating from the Eastern, Western, and Central Sahara and the Middle East. Combining ground-based AERONET sun photometers (24 stations), satellite (IASI, MODIS MIDAS) dust optical depth (DOD) data, and HYS-PLIT back-trajectories, we track these events across multiple Mediterranean sites. Results reveal clear regional differences in dust optical properties, such as aerosol optical depth, single scattering albedo, and asymmetry factor, arising from source regions and transport processes. Saharan events are dominated by coarse, scattering mineral dust, while the Middle East event featured finer, more absorbing particles, likely influenced by anthropogenic sources. MIDAS DOD-to-AOD ratios indicate that only one East-Central Saharan event maintained high dust fractions (DOD-to-AOD > 0.8), suggesting relatively pure dust, while other events exhibited stronger spatial variability, with the Middle East event showing the lowest ratios, reflecting enhanced mixing with anthropogenic or marine aerosols. A regional case study in Cyprus using in situ elemental and absorption measurements shows that Middle East dust, despite lower mass concentrations, exhibits stronger absorption than Saharan dust. METAL-WRF mineralogical simulations indicate broadly similar dominant mineral fractions (silicates and calcium-rich minerals) across events, suggesting that optical variability was mainly driven by dust-to-total aerosol ratio and mixing state rather



15 than mineralogy. UAV-based composition data further validate modeled variability, although discrepancies in aluminum and magnesium highlight limitations in current dust representations.

## 1 Introduction

Dust particles, referred to as dust henceforth, significantly influence climate (Kok et al., 2023), energy production systems (Kosmopoulos et al., 2018; Masoom et al., 2021), aviation (Ryder et al., 2024), and health globally (Proestakis et al., 2025), as these particles can travel vast distances from their source, often reaching locations thousands of kilometres away (Mona et al., 2023; Monteiro et al., 2022). The effect of dust, absorbing and scattering solar radiation, depends on its optical and physical properties (Adebiyi et al., 2023; Ito et al., 2021), which vary with its source region. These properties also determine whether dust will act as cloud condensation nuclei (CCN; Hatch et al., 2008) or as ice-nucleating particles (INPs; DeMott et al., 2009; Marinou et al., 2019), thereby affecting cloud development and precipitation (Casquero-Vera et al., 2023). During transport, dust composition and morphology can evolve due to aging and mixing with other aerosol types. For instance, Prospero (1999) noted that dust can carry pollutants, altering its composition and amplifying its environmental and health impacts. Size-segregated analyses also show that dust from different sources may evolve differently, with temporal changes in mineralogy driven by processes like gravitational settling (Di Biagio et al., 2023; Ebert et al., 2009).

The Sahara Desert in northern Africa and the Rub' al Khali in the Arabian region rank among the most significant dust-emitting regions worldwide. The Mediterranean region, due to its proximity to these desert regions, is heavily influenced by dust transport, leading to pronounced changes in aerosol loading and regional radiative balance, primarily under the prevalence of cyclonic systems (Gkikas et al., 2013, 2014, 2016; Flaounas et al., 2015; Marinou et al., 2017). Zittis et al. (2022) identified that aerosol radiative forcing in this area is one of the highest on a global scale. Dust transport from the Sahara to the Mediterranean follows distinct seasonal patterns, with activity typically peaking in spring over the eastern basin and in summer over the western basin (Mateos et al., 2015; Raptis et al., 2020). However, recent observations show a notable increase in winter dust inputs in Western Mediterranean, particularly in February and March, with unprecedented dust transport observed between 2020 and 2022 (Cuevas-Agulló et al., 2024). In parallel, research on Middle Eastern dust events points to a rise in storm frequency, attributed to land use changes that have generated new emission sources (Papi et al., 2022; Al Ameri et al., 2019). These sources are particularly significant because dust reaching the Mediterranean from the Middle East is often mixed with anthropogenic pollution, such as carbonaceous particles and trace metals (Teri et al., 2025; Bimenyimana et al., 2023). The Mediterranean's complex aerosol mixture, comprising of dust, sea salt particles, and continental aerosols, makes the region highly relevant for radiative closure studies (Papachristopoulou et al., 2022).

Beyond radiative effects, dust significantly impacts both marine and terrestrial ecosystems due to its influence across multiple physical, chemical, and biological processes. Dust deposition over sea can provide essential nutrients for phytoplankton growth (Rodríguez et al., 2023). On land, dust alters soil composition, affecting crop yields and agricultural productivity (Middleton, 2024). However, extreme dust events disrupt aviation, energy production, and infrastructure, leading to substantial economic losses (Cuevas et al., 2021). In addition, high concentrations of airborne dust exacerbate respiratory disease (De Longueville



et al., 2010; Goudie, 2014; Mid) and increase hospital admissions. In southern Europe, frequent dust outbreaks often exceed the World Health Organization (WHO) and the European Union (EU) air quality thresholds, including when mixed with pollutants and bioaerosols (Querol et al., 2019; Proestakis et al., 2025).

Despite its notable importance, only few studies have specifically focused on the evolution of dust optical and chemical properties during atmospheric transport in the Mediterranean, whilst measurements to support this research remain limited (Zender et al., 2004; Textor et al., 2006; Mahowald et al., 2014) with more recent work further addressing this gap (Gkikas et al., 2021; Logothetis et al., 2021; Gkikas et al., 2022; González-Romero et al., 2023; Castellanos et al., 2024). As a result, our understanding of the underlying processes, such as deposition and aggregation, is still poor. In addition, there is limited discussion of the impact of dust mixing with other aerosol types in relation to dust origin and transport pathways. The primary tools available for studying this evolution at high temporal and spatial resolution are satellite and ground-based remote sensing, including lidars (Papayannis et al., 2008; Balis et al., 2004; Amiridis et al., 2005) as well as atmospheric-dust regional models (Pérez et al., 2006; Gkikas et al., 2018). The AEROSOL ROBOTIC NETWORK (AERONET; <https://aeronet.gsfc.nasa.gov/>; last access: 06/02/2026), a globally distributed network of sun photometers, provides long-term, quality-assured observations of column-integrated aerosol properties (Holben et al., 1998). In the Mediterranean region, AERONET has a relatively dense coverage, with over 40 stations having recorded at least one full annual cycle between 2015 and 2025.

Through the analysis of measured aerosol properties with respect to dust origin and transport pathways, this study aims to assess the influence of transport processes, including aerosol mixing. To address these gaps, this study examines the optical and mineralogical properties of dust during four dust episodes over the Mediterranean Basin in 2021–2022. The approach of this paper is to combine ground-based and satellite-based remote sensing observations to assess the optical properties of dust. In addition, the mineralogical signature of dust will be studied through ground and unmanned aerial vehicle (UAV)-based in situ observations along with simulations.

The study is structured in three main parts. In the second section, the datasets and methodology used for the identification and characterization of the events is described. Section 3 presents the four selected dust events, describing their temporal and geographical extent, transport pathways, and main optical characteristics. Following, in the results section, the optical properties of aerosols measured at various AERONET stations impacted by each event are compared to understand the evolution of dust optical properties within single events and to assess how different dust sources influence the optical characteristics. The dust fraction at each station is evaluated using the MODIS Dust Aerosol (MIDAS) dataset described by Gkikas et al. (2021) to better characterize the aerosol mixture at each location. A further analysis using ground-based observations has been developed, focusing on the island country of Cyprus, which lies at the crossroad of three continents (Asia, Africa, Europe) and is the only area in Europe affected by both Saharan and M. East dust sources. As a result, Cyprus was affected by three of the four dust events considered, which allows the investigation of aerosol mixtures and mineralogical composition using ground-based observations from the Cyprus Atmospheric Observatory in Agia Marina Xyliatou. Finally, to understand how dust transport and different sources influence mineralogical composition, the METAL-WRF model (Solomos et al., 2023) is utilized. The mineralogical composition simulated by METAL-WRF is compared with UAV-based observations in Cyprus to assess the simulated dust composition during these events.



## 2 Data and Methodology

### 2.1 Global Datasets and Models

#### 85 2.1.1 AERONET

AERONET (AErosol RObotic NETwork) is a global network of ground-based sun–sky photometers that provides aerosol optical and radiative properties of more than 200 sites around the globe (Giles et al., 2019; Zhang et al., 2025). The most widely used product of AERONET is the spectral aerosol optical depth (AOD), which is derived from direct sun irradiance measurements at wavelengths from 440 to 1640 nm and is proportional to the amount of aerosol in the atmospheric column.

90 The spectral dependency of the AOD is expressed in terms of the scattering Ångström exponent (AE), which is an indicator of the aerosol particle size. In addition, AERONET measures sky radiances at different sky geometries, which are used in combination with AOD measurements to retrieve microphysical and optical aerosol properties using inversion algorithms (Sinyuk et al., 2020; Dubovik and King, 2000; Dubovik et al., 2000). Its long-term, high-quality, and globally distributed observations have been instrumental in studying dust variability and aerosol properties across diverse regions (Dubovik et al.,  
95 2002; Kim et al., 2011).

In this study, data products from Level 1.5 Version 3.0 (v3) AERONET retrievals (Giles et al., 2019) have been used. This decision is made against Level 2 data in order to achieve better data availability. For Level 1.5 products, as full re-calibration may not yet have been applied, we expect slightly larger uncertainties than Level 2.0. (0.01–0.02), with more relative impact in low AOD cases. AOD and AE data are primarily used to identify intense dust events in the Mediterranean basin. In addition,  
100 some inversion properties like the single scattering albedo (SSA), asymmetry parameter (ASY), and particle size distribution (PSD) are further analyzed to examine the evolution of the optical and microphysical aerosol properties.

More specifically, ASY is the integral of the energy distribution (phase function) weighted by the angle of scattering. Its value varies between -1 and 1, depending on whether the scattering is perfectly backward or forward with respect to the direction of incidence. It takes the value of zero in the case of isotropic scattering, which would correspond to scattering from gas molecules  
105 (Rayleigh scattering). For dust particles, which are 3 orders of magnitude larger in size, typical values are between 0.6 and 0.8 (e.g., Hess et al., 1998). The asymmetry factor is wavelength-dependent, providing insight into aerosol size and type. Higher values of the asymmetry parameter are associated with the presence of larger particles (Zeb et al., 2024).

SSA describes the scattering efficiency of particles, such as aerosols or clouds, relative to the total extinction (scattering + absorption) of light. Particles with  $SSA \approx 1$ , e.g., like sulfate aerosols, reflect sunlight and have a cooling effect, while highly  
110 absorbing particles ( $SSA \approx 0.2$ ), such as black carbon, contribute to warming by converting sunlight into heat. Aerosols with intermediate properties, like organic carbon or dust, can have varying climate direct impacts depending on their altitude and the surface albedo underlying them.

Finally PSD provides a quantitative description of aerosol concentrations across different particle sizes, which is important for understanding the mixture of fine and coarse particles during dust events.

115 For the inversions, the residual sky error was selected to be less than 6%. A higher value for the sky error value than the



commonly used 5% threshold is chosen, as it is observed that 5% cuts off a significant number of valid retrievals, as also mentioned in Holben et al. (2006).

### 2.1.2 ModIs Dust AeroSol (MIDAS) dataset

The MIDAS dataset, a MODIS-based dust aerosol product described by Gkikas et al. (2021), provides global estimates of dust optical depth (DOD) on a high-resolution  $0.1^\circ \times 0.1^\circ$  grid. It is derived from MODIS-Aqua (and more recently MODIS-Terra) AOD retrievals, combined with dust fraction information from the MERRA-2 reanalysis. The original dataset spanned from 2003 to 2017 and has recently been extended to 2023. Only high-quality MODIS retrievals are used, after filtering for cloud contamination and applying standard quality assurance criteria. Validation of the dataset was performed through comparison with AERONET observations, showing strong agreement and minimal bias. This validation confirms the accuracy of the MIDAS product in representing dust aerosols, particularly over key dust regions such as North Africa and the Middle East. MIDAS offers significant advancements compared with existing datasets, with higher spatial resolution and more accurate dust-specific retrievals. Since its development, the dataset has been applied across a range of studies, including studies on dust climatology (Gkikas et al., 2022; Logothetis et al., 2021) to modeling of emission and transport processes (Kiriakidis et al., 2023), as well as studies of dust impacts on solar energy production (Masoom et al., 2021; Papachristopoulou et al., 2022).

In this study, MIDAS is used to map the spatial extent and intensity of selected dust events over the Mediterranean by calculating daily mean DOD and AOD values at 550 nm at  $0.1^\circ \times 0.1^\circ$  resolution. These observations support the identification of the most affected regions and enable estimates of the dust fraction in the total aerosol load through DOD-to-AOD ratios. Maps of DOD overlaid with station locations are shown in Appendix C.

### 2.1.3 METAL-WRF

To complement the observational analysis, we employ the METAL-WRF modelling system, which simulates the distribution of dust mineral fractions in the atmosphere (Solomos et al., 2023). METAL-WRF couples the GOCART-AFWA dust emission scheme with prognostic tracers for nine mineral species—illite, kaolinite, smectite, calcite, quartz, feldspar, hematite, gypsum, and phosphorus—plus iron. Mineral fractions of the source regions are taken from the high-resolution GMINER30 (Nickovic et al., 2012) and FERRUM30 (Nickovic et al., 2013) databases. In the model, each mineral is treated as an independent prognostic scalar (Solomos et al., 2023), allowing its full life cycle—emission, transport, gravitational settling, diffusion, and wet scavenging—to be explicitly resolved. This approach enables the airborne mineral mixture to evolve both spatially and temporally, producing spatially explicit fields of mineral-specific dust mass that can be used to trace source fingerprints and their evolution during Mediterranean transport.



## 2.2 In Situ Measurements at Cyprus Atmospheric Observatory (CAO)

### 145 2.2.1 Ground-based

The study uses ground-based in situ measurements recorded at the Cyprus Atmospheric Observatory (CAO) in Agia Marina Xyliatou, operated by the Climate and Atmosphere Research Centre (CARE-C) of the Cyprus Institute (CyI), to compare dust concentrations, elemental composition, and dust absorption during these events.  $PM_{10}$  and  $PM_{2.5}$  were measured at Agia Marina Xyliatou using pre- and post-weighted filters, providing insights into the temporal variation of the particulate matter (PM) levels. Applying acid digestion on integrated daily samples combined with inductively coupled plasma-mass spectrometer (ICP-MS) analysis on parts of the samples, the elemental composition could be directly estimated (Bimenyimana et al., 2023). Based on the method described in Querol et al. (2001), dust concentrations were estimated by indirectly calculating Si and  $CO_3^{2-}$  using the following empirical relationships:

$$SiO_2 = 3 \times Al_2O_3 \quad (1)$$

155

$$CO_3^{2-} = 1.5 \times Ca + 2.5 \times Mg \quad (2)$$

The absorption coefficient for the dust events is calculated using observations from two Aethelometers instruments (model AE33, Magee Scientific, USA) installed at CAO Agia Marina Xyliatou. The AE33 determines the light attenuation coefficient ( $b_{ATN}$ ) by continuously collecting particles on a filter tape and measuring the change in optical transmission between a clear and a clean part and a sampled spot.

Two different inlet configurations were used to investigate size-resolved absorption properties. One AE33 was equipped with a  $PM_1$  cyclone providing the submicron absorption coefficient. The second instrument was connected to a virtual impactor (VI), which enhances the coarse particle fraction by concentrating particles larger than approximately  $2.5 \mu m$  in the minor flow. This setup allows the characterization of dust-dominated absorption associated with coarse-mode particles.

165 The dust absorption is then defined by subtracting the submicron absorption from the VI absorption following the methodology described in Drinovec et al. (2020):

$$b_{abs, PM_{10-1}} = \frac{b_{abs, VI} - b_{abs, PM_1}}{EF} \quad (3)$$

, where EF is the enhancement factor describing the enrichment of the coarse fraction in VI.

### 2.2.2 UAV-based

170 During the 2021 Cyprus Fall Campaign, carried out from October 18 to November 18, the Unmanned Systems Research Laboratory (USRL, Kezoudi et al.2021a) of the Cyprus Institute (CyI) utilized UAVs equipped with advanced instruments like OPCs and impactors to collect samples, alongside ground-based remote sensing and in situ instrumentation of the CAO of



the CyI. The study investigated the microphysical and optical characteristics of mineral dust transported over Cyprus. For the sample collection at different altitudes, a 3D-printed miniaturized version of the Giant Particle Collector (GPAC or impactors) was deployed on the UAVs. Overall, the Scanning Electron Microscope (SEM) analysis of these samples identified silicates as the dominant component, with Ca-rich materials and clay minerals also present in significant proportions.

### 2.3 Heights, Trajectories and Origin Analysis

In addition to the information provided by the different datasets mentioned, the heights, trajectories, and origin of the different aerosol events were analyzed as well.

#### 2.3.1 EARLINET

The vertical distribution of dust particles was estimated using European Aerosol Research Lidar Network (EARLINET; Pappalardo et al., 2014) measurements from stations co-located with or located sufficiently close to the AERONET sites listed in Tab. 1, performed on the peak date of the event, as reported in the same table. For each measurement, the particle backscatter coefficient and the particle depolarization ratio were used to retrieve the dust backscatter coefficient profile. In particular, the dust component was separated from the total aerosol backscatter profile based on depolarization ratio values, following the methodology described by (Tesche et al., 2009). The altitude of the dust layer was then determined by identifying the level at which the dust backscatter coefficient reached its maximum value, indicating the highest dust concentration (see Appendix A).

#### 2.3.2 LIVAS

Aerosol optical properties profiles provided by Cloud–Aerosol Lidar with Orthogonal Polarization (CALIOP), the primary instrument onboard the Cloud–Aerosol Lidar and Infrared Pathfinder Satellite Observations (CALIPSO; Winker et al., 2010) satellite, were applied under a similar approach, towards addressing the four-dimensional structure of dust aerosol layers transported over the broader Mediterranean region. More specifically, vertical profiles of dust extinction coefficient at 532 nm and total aerosol particulate depolarisation ratio at 532 nm, as well as peak height of the atmospheric dust component along the CALIPSO orbit path, were extracted by the European Space Agency (ESA) “Lidar climatology of Vertical Aerosol Structure” (LIVAS) dust climate data record (Amiridis et al., 2013, 2015; Marinou et al., 2017; Proestakis et al., 2018, 2024; Aslanoğlu et al., 2022) and analysed as in the example seen in Fig. B1 (see Appendix B).



### 2.3.3 IASI-MAPIR

The IASI-MAPIR dataset (version 5.11, available at <https://doi.org/10.18758/f7el2zbr>) was used to independently identify and characterize the dust events. Specifically, the retrieved dust vertical profiles and integrated dust AOD were employed to (i) confirm the presence of mineral dust over the study region, (ii) determine the spatial extent of the dust plumes, and (iii) estimate the altitude of the dust layers upon arrival at the affected stations (Appendix D).

The dataset is particularly valuable because the thermal infrared retrieval allows direct separation of mineral dust from other aerosols without requiring post-processing. Although subject to some limitations in quality control (e.g., the data set is "cloud-free" only, sensitivity is reduced at low AOD, and when the surface and the dust layer are at similar temperatures), these data contribute valuable insight into the intensity, spatial spread, and vertical extent of dust plumes at the affected stations.

210

### 2.3.4 HYSPLIT

The Hybrid Single-Particle Lagrangian Integrated Trajectory (HYSPLIT) model (Stein et al., 2015; Rolph et al., 2017) was run with using Global Data Assimilation System (GDAS) meteorological reanalysis fields at approximately 50 km resolution to investigate the trajectories of observed air masses over the stations affected by dust events. Grid ensemble 120-hour backtrajectories were computed from each station arriving at the date, time, and altitude of the observed dust event. A set of trajectories is automatically calculated around a cube (3-dimensional), centered on the initial point. The cube comprises 27 points across three planes, with nine trajectories per plane located at a vertical spacing of  $\pm$ . The horizontal spacing of these trajectories is  $1^\circ$  in latitude ( $\sim 111$  km) and  $1^\circ$  in longitude ( $\sim 111$  km  $\cdot$  cosine latitude).

215

## 3 Event Identification

Using the tools described in the previous section, the following methodology was applied to determine the dates for analysis, select relevant stations, and classify data sources.

The first step was to identify significant dust events across the Mediterranean Basin using AERONET observations in the years 2021-2022 from all the stations in the area. Dust episodes were identified based on two concurrent criteria on daily averaged data from AERONET:

225

- AOD at 500 nm  $> 0.2$  and
- AE between 380–500 nm less than 0.3.

IASI pure dust satellite AOD retrievals were also analysed to complement this information in order to ensure that the aerosol type could be classified as mineral dust (Appendix D).

Using these thresholds, spatial maps were generated to identify 20-day periods during which dust impacted over 10 AERONET stations. These maps allowed us to highlight widespread dust activity across the region.

230

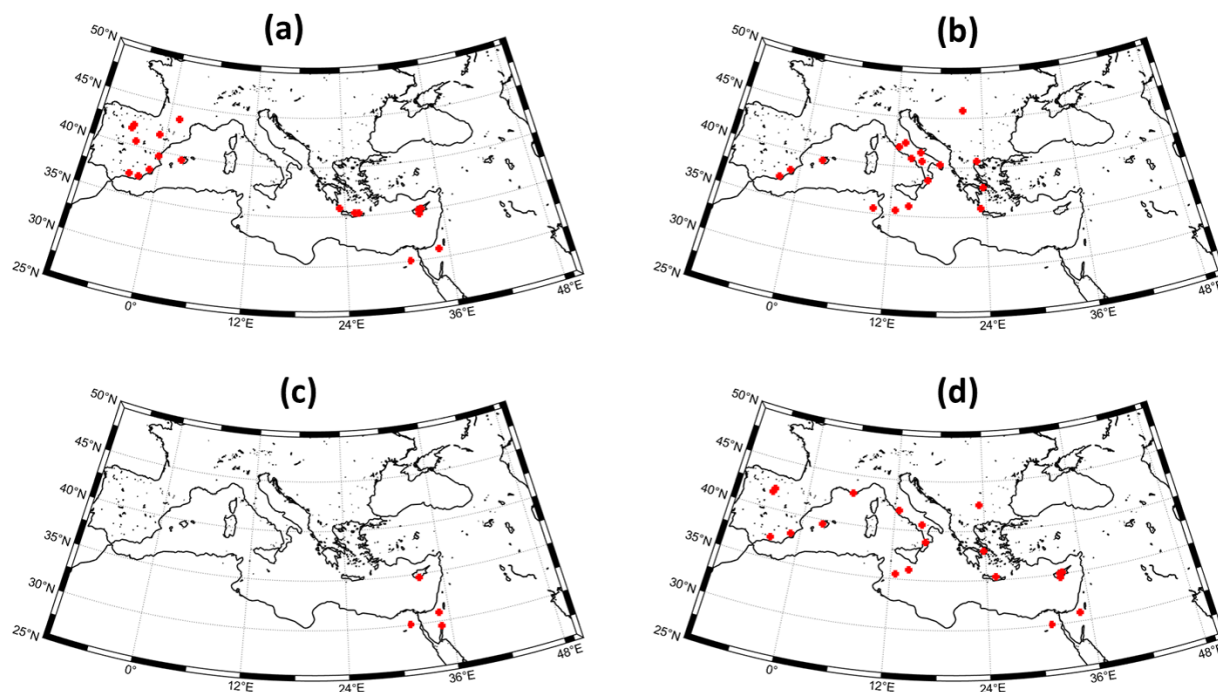


**Figure 1.** Map of AERONET stations where AOD > 0.2 and (ii)  $-0.1 < AE < 0.3$  between a) 18th and 29th March 2021, b) 17th and 28th June 2021, c) 10th and 21th November 2021, and d) 20th April and 10th May 2022.

Figure 1 shows four selected cases where dust influenced several stations across the Mediterranean basin. During the first event (Fig. 1a), intense dust influenced both the Eastern Mediterranean and the Iberian Peninsula between 18 and 29 March 2021. This study focuses only on the Eastern Mediterranean part of this event, as the associated dust plume followed a more clearly traceable transport pathway across the Mediterranean. According to IASI, the event originated over Algeria, subsequently moving eastward across the Mediterranean Sea and reaching the Eastern Mediterranean (fig. D1a). The AOD levels were relatively high along the transport path, particularly over the Central Mediterranean and near the affected stations, indicating a dense and well-developed dust plume. The mean altitude appeared to be relatively low, about 3km (fig. D2a).  
In the second event, stations in the Central Mediterranean and Central Europe were affected (Fig. 1b). The outbreak appears to have originated over northern Algeria and Tunisia, before moving northeastward across the Central Mediterranean Sea. The IASI-derived AOD indicated enhanced dust loads, with the most affected areas being in the Central Mediterranean and parts of southern Italy and Greece (fig. D1b). The mean altitude for this event ranged between 4 to 5 km, suggesting efficient long-range



transport in the mid-troposphere and a well-developed dust plume extending over a wide area (fig. D2b).

The third event was weaker and more localized affecting only the Eastern Mediterranean and the Middle East (Fig. 1c). AOD values were generally lower than in the previous events, and the spatial extent of the plume was limited (fig. D1c). This event  
245 originated from the Middle East, affecting mainly the Eastern Mediterranean. The mean altitude remained lower than in the previous events, between 2 to 3 km, indicating a more confined plume, possibly due to less intense uplift or less favorable transport conditions (fig. D2c).

Finally, the fourth event on the other hand, affected more than ten stations spanning from the Eastern to the Western Mediterranean (Fig. 1d). According to HYSPLIT backtrajectories, the latter was composed of multiple successive sub-events: the first  
250 originated over the Tunisia–Libya region and impacted Central and Eastern Europe; this was followed by a Middle Eastern dust outbreak affecting parts of Eastern Europe; finally, a plume emerging from the Tunisia–Algeria region was transported toward Western Europe. Overall, the main dust activity appears to have originated from Algeria and Libya, and shows moderate AOD levels as the dust travels eastward across the Mediterranean according to IASI (fig. D1d). The mean altitude was approximately 3 km, comparable to event A, but the broader distribution and slightly higher altitude suggest a moderate-intensity event with  
255 widespread influence across the basin (fig. D2d).

A more detailed analysis was performed to determine the exact timing of the dust events and the origins of the dust plumes. A visual inspection of AERONET products was conducted to pinpoint the specific dates of the dust episodes with increased accuracy. The detailed analysis is based on selected stations affected during each event, ensuring broad spatial coverage across the region, based on the availability of sufficient inversion data (e.g., size distribution, asymmetry factor, single scattering albedo),  
260 with preference given to those providing lidar or ceilometer observations to capture the vertical variability of the dust layers during transport. The arrival height of the dust plumes was estimated using co-located vertical profile observations, where available (e.g., from ACTRIS/EARLINET lidar instruments). It should be emphasized that in the case of Cyprus, three stations are equipped with instrumentation providing the observations relative to the vertical structure of the dust layers (CUT-TEPAK, Agia Marina Xyliatou, and Nicosia), and therefore, the selection of the most suitable station was based on the retrieval avail-  
265 ability.

Table 1 provides an overview of the dust events in the period 2021–2022 and the corresponding stations selected for analysis in the framework of the present study. The peak date refers to the day with the highest AOD during the main dust event identified in each period. In cases where two sub-events occurred within the same period, only the most intense (in area and AOD) is considered. Maximum and minimum AODs for the peak date are also provided in the table. The stations are numbered in  
270 ascending order (from 1 to 6) based on their distance from the source, from the nearest to farthest. For specific events (like event D), the sequence was not clear due to the multiple occurring events, and the numbering may not accurately reflect the actual station's distance from the source.

To confirm the diversity of the origin and transport pathways of the dust plumes, we conducted trajectory analysis using the HYSPLIT model. The resulting back trajectories, illustrated in Fig. 2, depict the transport pathways at two representative  
275 stations affected during each event and provide the origins shown in Table 1.

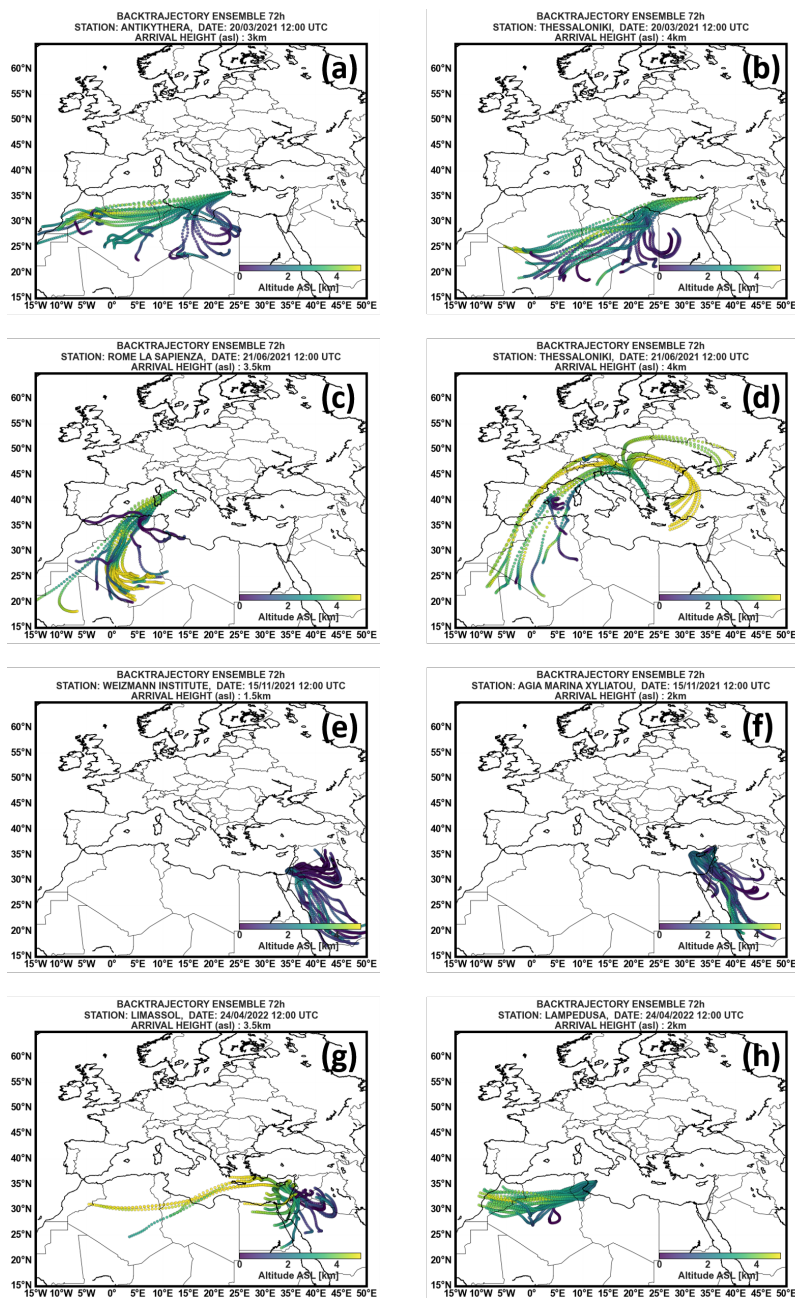


**Table 1.** Selected dust events along the Mediterranean Basin during the period 2021-2022. Stations are listed in ascending order according to the sequence in which they were affected by each dust event. The minimum and maximum AOD values correspond to the instantaneous values recorded on the peak day of the event at each station.

| Event A   |   |         |         |           | Event B                                    |         |         |           |
|-----------|---|---------|---------|-----------|--|---------|---------|-----------|
| Dates     |   |         |         |           | 17-28/06/2021                              |         |         |           |
| Origin    |   |         |         |           | Western Sahara                             |         |         |           |
|           |   | MAX AOD | MIN AOD | Peak Date |  | MAX AOD | MIN AOD | Peak Date |
| Station 1 | Cairo, Egypt<br>(30.1°N, 31.3°E)        | 0.96    | 0.61    | 22/3/2021 | Ben Salem, Tunisia<br>(35.6°N, 9.9°E)      | 0.91    | 0.50    | 21/6/2021 |
| Station 2 | Sede Boker, Israel<br>(30.9°N, 34.8°E)  | 1.40    | 0.90    | 24/3/2021 | Rome, Italy<br>(41.9°N, 12.5°E)            | 1.09    | 0.60    | 21/6/2021 |
| Station 3 | Finokalia, Greece<br>(35.3°N, 25.7°E)   | 0.76    | 0.11    | 22/3/2021 | Antikythera, Greece<br>(35.9°N, 23.3°E)    | 0.87    | 0.55    | 22/6/2021 |
| Station 4 | Antikythera, Greece<br>(35.9°N, 23.3°E) | 0.50    | 0.25    | 22/3/2021 | Athens, Greece<br>(38.0°N, 23.7°E)         | 1.18    | 0.60    | 22/6/2021 |
| Station 5 | CUT-TEPAK, Cyprus<br>(34.7°N, 33.0°E)   | 1.46    | 0.42    | 22/3/2021 | Thessaloniki, Greece<br>(40.6°N, 23.0°E)   | 1.48    | 0.59    | 22/6/2021 |
| Station 6 | Nicosia, Cyprus<br>(35.1°N, 33.4°E)     | 1.05    | 0.23    | 22/3/2021 | Magurele-Inoe, Romania<br>(44.3°N, 26.0°E) | 0.50    | 0.27    | 25/6/2021 |

| Event C   |  |         |         |            | Event D                               |         |         |           |
|-----------|--|---------|---------|------------|---------------------------------------|---------|---------|-----------|
| Dates     |  |         |         |            | 21/04-01/05/2022                      |         |         |           |
| Origin    |  |         |         |            | West, East and Central Sahara         |         |         |           |
|           |  | MAX AOD | MIN AOD | Peak Date  |                                       | MAX AOD | MIN AOD | Peak Date |
| Station 1 | Sede Boker, Israel<br>(30.9°N, 34.8°E)           | 0.49    | 0.31    | 14/11/2021 | CUT-TEPAK, Cyprus<br>(34.7°N, 33.0°E) | 0.99    | 0.44    | 24/4/2022 |
| Station 2 | Cairo, Egypt<br>(30.1°N, 31.3°E)                 | 1.02    | 0.44    | 14/11/2021 | Athens, Greece<br>(38.0°N, 23.7°E)    | 0.60    | 0.1     | 25/4/2022 |
| Station 3 | Weizmann Institute, Israel<br>(31.9°N, 34.8°E)   | 0.66    | 0.40    | 14/11/2021 | Rome, Italy<br>(41.9°N, 12.5°E)       | 0.76    | 0.08    | 23/4/2022 |
| Station 4 | Agia Marina Xyliatou, Cyprus<br>(35.0°N, 33.1°E) | 0.31    | 0.20    | 15/11/2021 | Mallorca, Spain<br>(39.6°N, 2.6°E)    | 0.90    | 0.07    | 26/4/2022 |
| Station 5 | IMS-METU-ERDEMLI, Turkey<br>(36.6°N, 34.3°E)     | 0.47    | 0.21    | 15/11/2021 | Lampedusa, Italy<br>(35.5N, 12.6°E)   | 0.80    | 0.11    | 25/4/2022 |
| Station 6 | Finokalia, Greece<br>(35.3N, 25.7°E)             | 0.31    | 0.25    | 17/11/2021 | Valladolid, Spain<br>(41.7N, 4.7W)    | 0.54    | 0.39    | 29/4/2022 |



**Figure 2.** 120-hour HYSPLIT Ensemble backtrajectories for the four selected events: event A (a, b), event B (c, d), event C (e, f), and event D (g, h). Each ensemble member is generated by applying a fixed grid offset to the meteorological data, highlighting the variability in transport pathways. Arrival heights are calculated based on vertical profiles from collocated lidar observations. The color scale along each trajectory represents altitude above sea level (km).



## 4 Results and Discussion

### 4.1 Aerosol Optical Properties and Size Distributions

Figure 3 shows the relation between AOD at 500 nm and AE 440-675 nm, for the peak date at each station, during each event, which combined provides insight on the intensity and composition of each of the events at different locations. The AE parameter provides aerosol particle size; the lower this parameter is the bigger the particle size. Coarse particles usually present AE values below 1 since they have a lower spectral dependency. In particular, values of  $AE < 0.3$  have been found for very high AOD Saharan aerosol dust events (Toledano et al., 2007; Valenzuela et al., 2015; Gkikas et al., 2009, 2013, 2016).

Observations are categorized into four aerosol types following the boundaries defined in Kalapureddy et al. (2009): desert dust, pollution, mixed aerosols, and background. The colour scheme in the plots corresponds to the direct distance of the affected stations from the source, with the closest station to the source shown in turquoise and the furthest in grey. The full sequence of colours is as follows: turquoise, green, orange, magenta, brown, and grey.

For event A (see Fig. 3a) a wide range of AOD values are observed reaching up to 1 for Cairo\_EMA\_2, Nicosia and CUT-TEPAK stations. Relatively similar AE values were observed in all stations on the peak day, with values below 0.5, indicating that a similar aerosol plume with large particles, classified as desert dust, was affecting these stations.

During event B (see Fig. 3b), the AOD and AE values remained above 0.5 and below 0.4, respectively, for almost all the stations, classifying the aerosols as desert dust. The only exception is seen for Magurele\_Inoe (Romania), where the significantly lower AOD values and higher AE suggest the presence of a more mixed or polluted air mass. This station exhibited a weaker response to the dust event, as also reflected in the time series of AOD and AE (Figs. E1b and E2b).

With respect to event C (see Fig. 3c), this event shows a lower intensity than the rest of the analyzed events, with AOD values  $\sim 0.4$ . In this case, AE is relatively high and constant (Fig. E2c) in all the stations, with values between 0.5 and 1.5, indicative of a mixed aerosol event likely influenced by both dust and anthropogenic pollution.

Event D (see Fig. 3d) is characterized by high AOD ( $>0.4$ ), for all the stations, AE reaches values close to when the maximum AOD occurs. Looking at the time series of this event (see Fig. E1d and E2d), it is noticeable that the event is characterized by high variability in terms of AERONET observations, possibly attributed to the significant geographical extent of the event, between Eastern and Western Mediterranean. Most observations are classified as desert dust, with only a few measurements at Palma\_de\_Mallorca (Eastern Spain) corresponding to background aerosol conditions.

Detailed time series of both AOD and AE are found in the Appendix E.

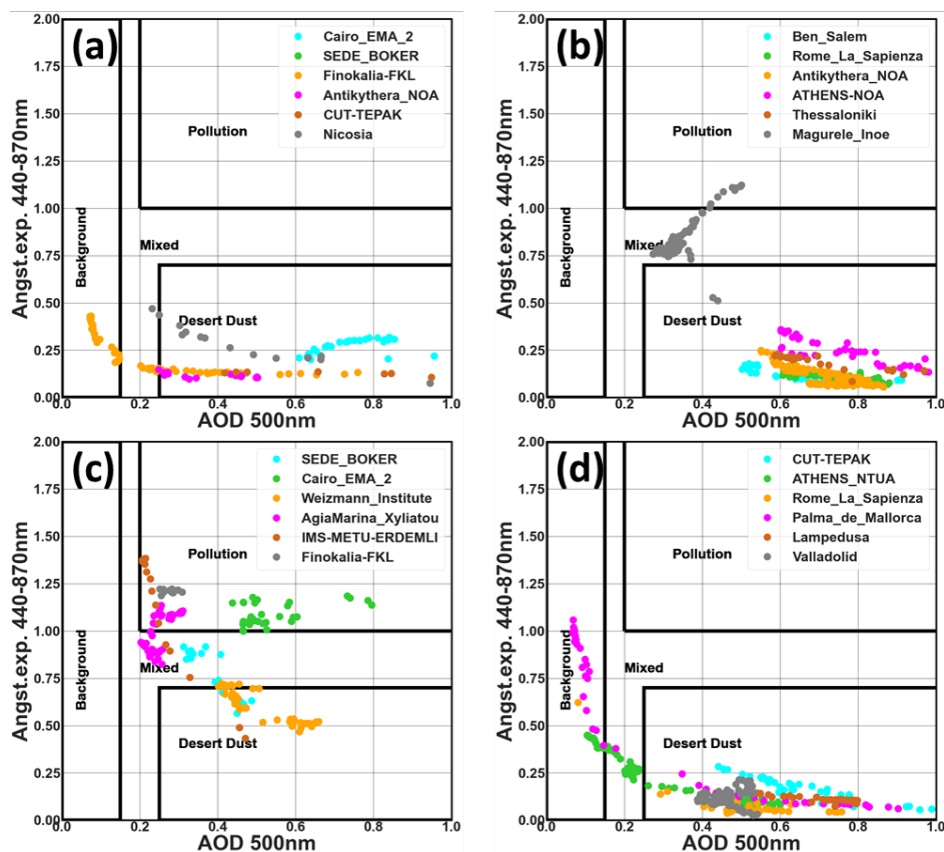


**Figure 3.** Scatter plots of Ångström exponent (440–870 nm) versus AOD at 500 nm for the four dust events: (a) event A, (b) event B, (c) event C, and (d) event D. Different colors denote the observations on the peak date at individual AERONET stations. The black lines indicate classification thresholds that separate the background, mixed, desert dust, and pollution-dominated aerosol regimes.

As a next step, the microphysical and optical aerosol properties retrieved by AERONET at the selected stations are discussed. The average of the retrievals that meet the criteria considered (see Sec. 2) are calculated for the day with the highest AOD value at each station for each event. Error bars with standard deviation are plotted for cases where more than one observation are available. For the Middle East and Central Sahara events, it was feasible to retrieve inversions only for some of the stations affected, as not all of the inversions were meeting the criteria.

The first parameter derived from inversion considered here is the asymmetry parameter. Figure 4 shows that the values of this parameter for these events are in the range expected for dust particles (0.6-0.8) (Korras-Carraca et al., 2015). Low ASY values are observed for all the stations affected by event C (originating from Middle East), comparable to those recorded at Magurele during event B and at CUT-TEPAK during event D. These reduced ASY values may be associated with the presence of smaller particles in the dust mixture observed at these stations. In the case of Magurele, the relatively lower ASY values observed can possibly be attributed to the elevated levels of continental aerosols and the lower amount of dust reaching this site. There is a strong wavelength dependence in all cases at shorter wavelengths. A similar ASY behavior is observed between



events A and B (originating from Eastern and Western Sahara, respectively). A wider spread in ASY is observed in the case of event D (originating from Central Sahara), which can be explained by dust particles of varying properties resulting from the wide source area these particles originated from initially.

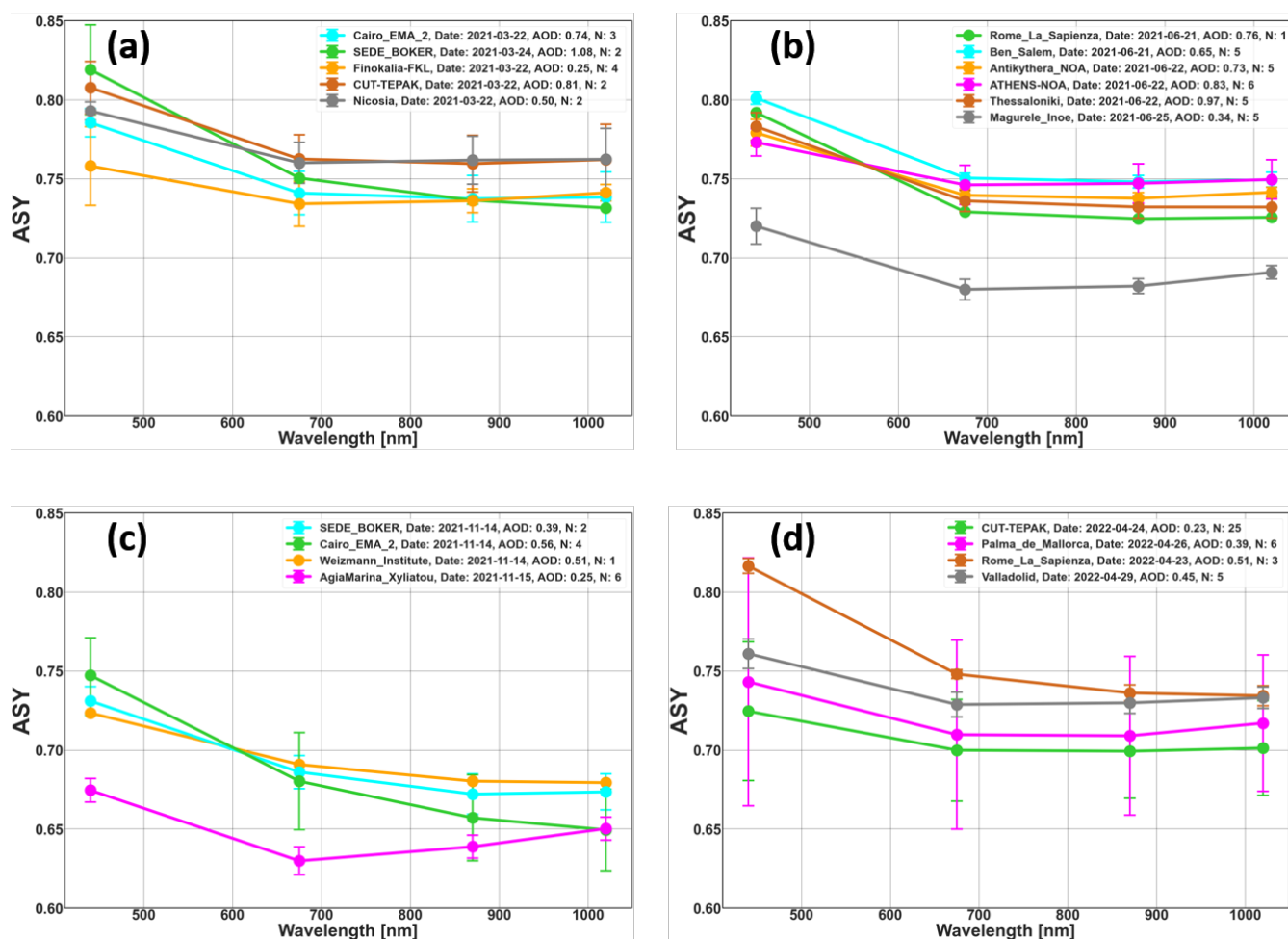


**Figure 4.** Daily averaged asymmetry factor (ASY) from AERONET inversion products (level 1.5, sky error < 5%) for all the events (A: March 2021, B: June 2021, C: November 2021, D: March 2022), for the day with the highest AOD of the events at each station. Error bars correspond to the standard deviation of the size distributions during the day. Legend shows which is the day with highest AOD for each station, the averaged AOD value for that day and the number of inversions available (N).

It is possible to compare the ASY values obtained for the same station for different source regions (different events). Small differences are observed for Rome, with event D showing a slightly stronger spectral dependence than event B. A more pronounced effect is observed at the Cairo station, where ASY values are significantly lower (indicating smaller particles) when the dust originates from the Middle East (event C) compared to the East and Central Sahara (event A). A similar reduction in ASY pattern is observed at CUT-TEPAK when comparing events A and D, where the station in the latter event is influenced by

320



325 Middle Eastern air masses, as shown in Fig. 2. This consistent pattern suggests that the observed ASY behavior, characterized by lower ASY values, is primarily driven by source characteristics (Middle East) rather than by local mixing effects at the measurement stations.

Another parameter derived from inversion that can give us information on the scattering properties of the dust events is the single scattering albedo.

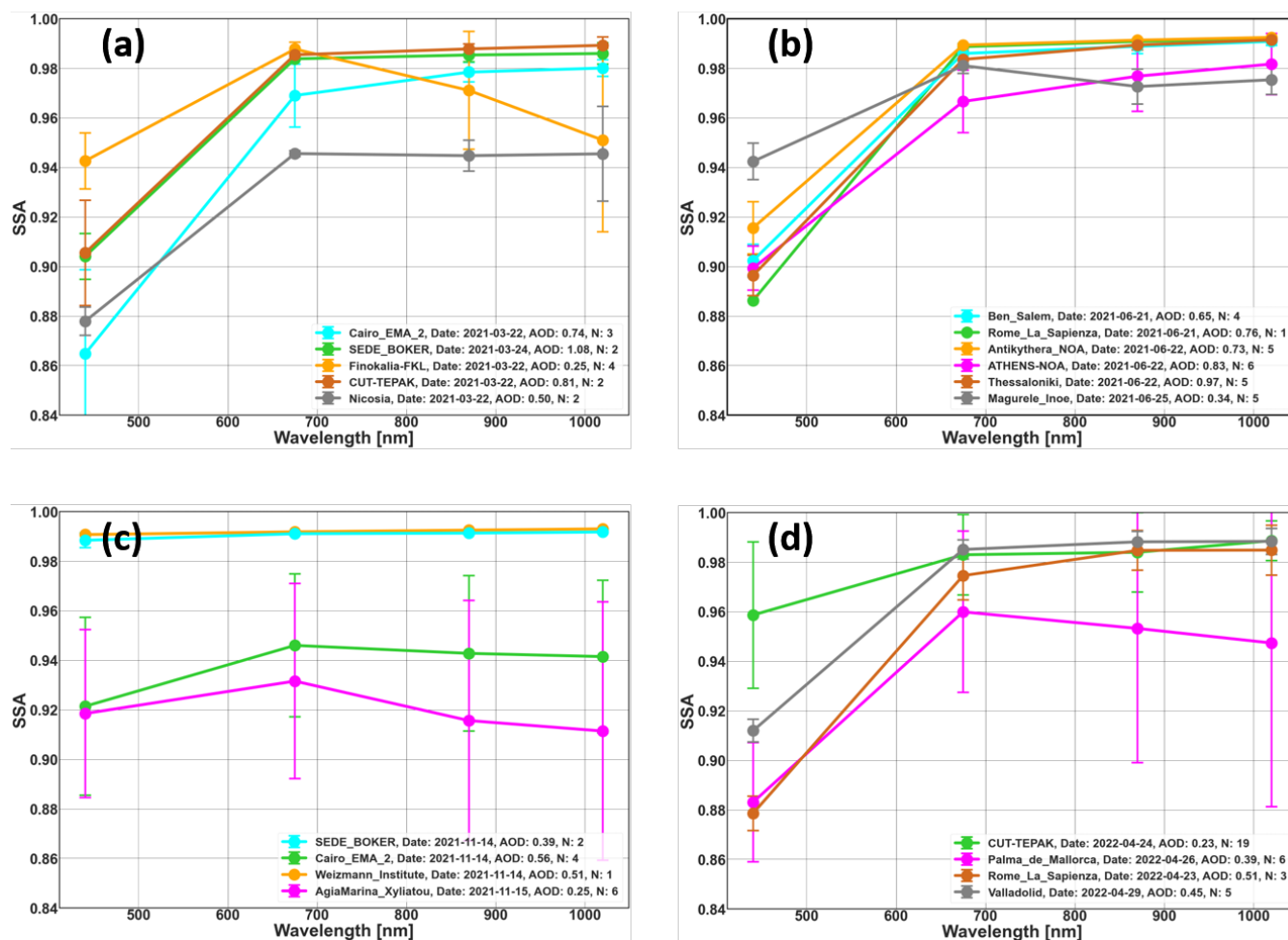


**Figure 5.** Daily averaged Single Scattering Albedo (SSA) from AERONET inversion products (level 1.5, sky error < 6%) for all the events (A: March 2021, B: June 2021, C: November 2021, D: March 2022), for the day with the highest AOD of the events at each station. Error bars correspond to the standard deviation of the size distributions during the day. Legend shows which is the day with highest AOD for each station, the averaged AOD value for that day and the number of inversions available (N).

330 In Fig. 5, the SSA values are shown for all the inversions that fulfil the criteria explained above, at each station, for all the events. In general, the observed values and wavelength dependence are consistent with those found in previous works



(Dubovik et al. (2002), Cachorro et al. (2010), Kim et al. (2011), Giles et al. (2012), Burgos et al. (2016)). For the three Saharan dust events (A, B and D), low values (0.86-0.94) are found around 440 nm wavelength, with higher values (0.94-0.99) at 675 - 1020 nm. During the Middle East event (C), Cairo and Agia Marina show relatively low SSA values ( $SSA \leq 0.94$ ), consistent with more absorbing particles. In contrast, Sede Boker and Weizmann display the highest SSA values observed across all events. HYSPLIT back-trajectories indicate that the air mass arriving at these two stations originated over inland Saudi Arabia and that other stations affected by the same airmass have also similar SSA behaviour (e.g., Technion\_Haifa\_IL, Israel and KAUST\_Campus, Saudi Arabia). This inland trajectory excludes significant marine influence, suggesting that sea salt aerosols are unlikely to explain the very high SSA observed ( $\sim 0.99$ ). Another speculation is that these inland trajectories are not affected by compaction while in the other cases the trajectories could be affected by combustion. Instead, the elevated SSA (also observed on 15 November 2021) may result from the presence of mineral dust with inherently low absorption or long-range transported dust internally mixed with secondary scattering aerosols, such as sulfates or nitrates. Such aging and coating processes are known to increase SSA significantly during transport as also described in Bauer et al. (2007). It should be noted that no level 2 data are available for the two stations on that date.

In the case of the East-Central Sahara event (A), it is noticeable that Nicosia has smaller values than the rest of the stations, especially when compared with CUT-TEPAK, which is the nearest. This suggests that there might be some local aerosol mixing with the dust, for example, through interaction with emissions from power stations in the outskirts of Limassol as the dust plume moves inland toward Nicosia. The decrease seen at Finokalia for longer wavelengths could be explained by the lower AOD values at Finokalia, since small variations in AOD can have a large effect on SSA retrievals (Andrews et al., 2017). In the Western Sahara event (B), there is less variability between stations, except for Magurele, which has a higher SSA at 440 nm.

For event D, there is high variability in SSA, especially at the shortest wavelength, where dust is mostly absorbing. Palma de Mallorca station and Rome have in overall, the lowest values at the 440nm wavelength indicating stronger absorption compared to other stations. Interestingly for Palma de Mallorca there is a decreasing trend of SSA at longer wavelengths, which, in combination with low AOD suggests locally mixed aerosols.

In Fig. 6 the fine-mode-fraction (FMF) product from AERONET at 500nm, which describes the proportion of fine-mode aerosol optical depth to the total aerosol optical depth, is compared to the averaged ASY and SSA parameters for the four events discussed in this study. This analysis provides insight into the relative contribution of fine absorbing particles and coarse mineral dust, allowing a clearer assessment of aerosol mixing processes during each event. In this comparison, event C originating from the Middle East stands out from the rest of the events, exhibiting the highest FMF ( $\sim 0.6$ ) and lowest ASY ( $< 0.75$ ). Although Event C does not exhibit enhanced absorption at 440 nm on average based on SSA, it shows the lowest average SSA at 675 nm among all events. However, these averages are influenced by the relatively high SSA values observed at the Weizmann and Cairo stations, which increase the overall event mean. In contrast, events A,B and D generally displayed lower FMF. These findings are further supported by the retrieved particle size distributions and the dust fractions derived from the MIDAS dataset, which confirm the increased fine-mode influence during event C.

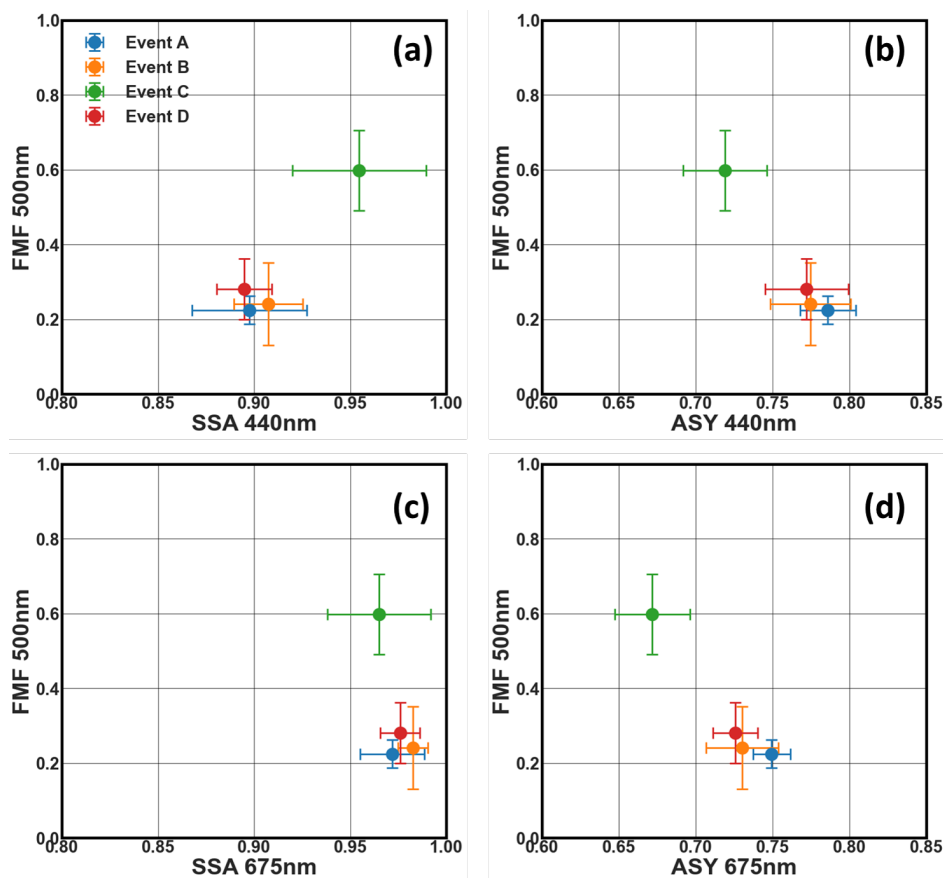


**Figure 6.** Comparison of FMF at 500 nm with (a,c) SSA at 440 and 675 nm and (b,d) ASY at 440 and 675 nm for different aerosol events. Data points represent the averaged values over all stations on their peak date during event A (blue), event B (orange), event C (green), and Event D (red), with horizontal and vertical error bars indicating uncertainties in the respective measurements.

365 Figure 7 presents the volume size distributions for each event, at the corresponding stations. For each station, the daily averaged size distribution on the day with the highest AOD is shown. It is important to note that the sky error criterion of < 6% is applied once again. Error bars correspond to the standard deviation of the size distributions during the day, when more than one observation is available.

370 For the East-Central Sahara event (A), the volume size distribution shapes are similar across different sites, with significant contribution by coarse-mode particles, with radius around  $2.24 \mu\text{m}$ . The concentrations of coarse particles are more prominent at sites closer to the source (Cairo and Sede Boker).

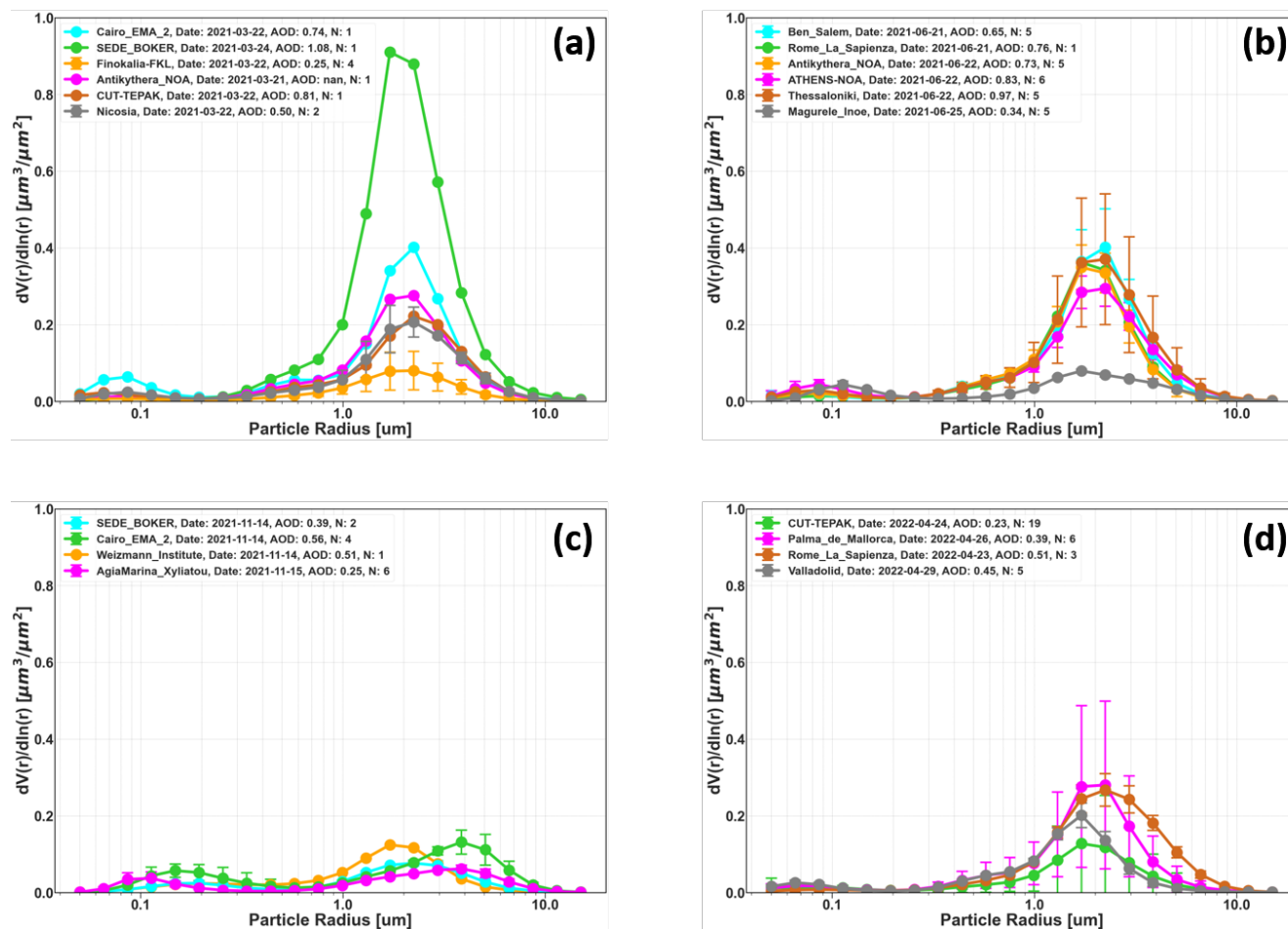


**Figure 7.** Daily averaged size distribution from AERONET inversion products (level 1.5, sky error < 6%) for all the events (A: March 2021, B: June 2021, C: November 2021, D: March 2022), for the day with the highest AOD of the events at each station. Error bars correspond to the standard deviation of the size distributions during the day. Legend shows which is the day with highest AOD for each station, the averaged AOD value for that day and the number of inversions available (N).

Notably, for Western and Central Sahara events (B and D), in which the stations are widely distributed across the Mediterranean, the size distributions at different stations exhibit similar shapes and values, particularly for the coarse mode, which is predominant in these events. One exception is at Magurele site in event B, where the coarse mode is not significantly higher than the fine mode, suggesting the possibility that fewer particles arrive due to deposition during transport, as it is the furthest station from the source. In both cases, the peak of the coarse mode is between 1.7-2.24  $\mu\text{m}$  while the concentrations at the peak are between 0.1-0.4  $\mu\text{m}^3/\mu\text{m}^2$  with no clear link between distance from source and concentration magnitude.

For the Middle East event (C), the volume concentration is lower at all the stations compared with the rest of the events, reflecting the lower overall AOD values, and there are notable variations in the size distributions among the sites. At all sites,



the coarse mode is dominant, however there is also a significant fraction of the fine mode, meaning that there is a mixture of different aerosols species. The radius for the maximum concentration value is found around  $1.7 \mu\text{m}$  except at Cairo station, which has the highest volume concentration and the peak corresponds to the radius value of  $3.86 \mu\text{m}$  (the highest amongst all events considered here), indicating significantly larger particles compared to the other stations affected by the same event.

## 385 4.2 Dust Fraction

To examine the contribution of dust to the total aerosol load, we estimated the DOD-to-AOD ratios based on the MIDAS dataset. For the DOD-to-AOD ratio, values close to 1 denote the sole presence of dust particles, while as the ratio decreases the contribution of other types (dust mixtures) in the specific event becomes more prominent. The ratios are estimated for each day of the four dust events with provided concurrent observations from AERONET stations (as per 1).

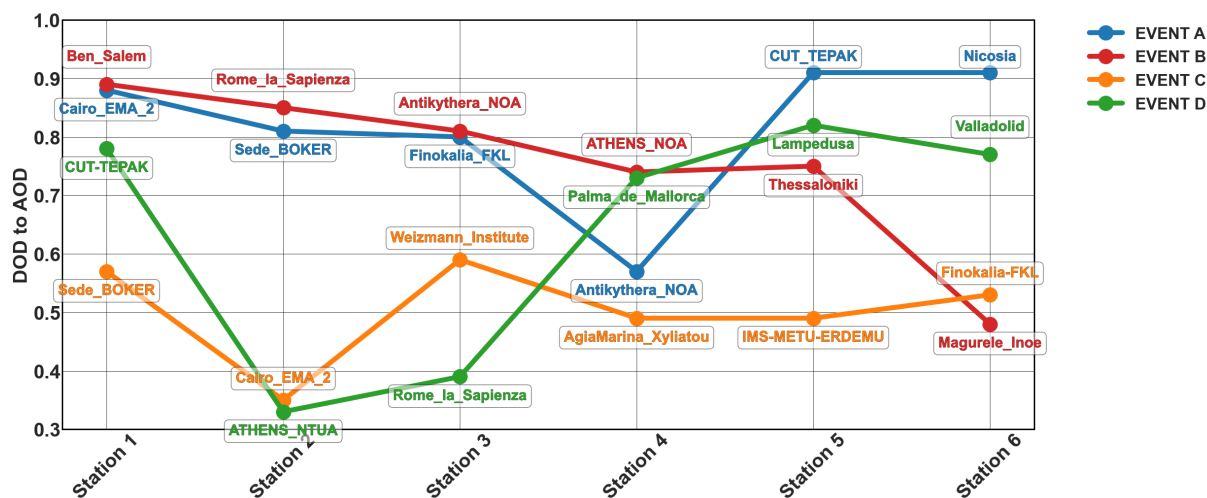


**Figure 8.** DOD-to-AOD ratios (at 550 nm) from MIDAS at the stations affected during events A-D shown in ascending order starting from the closest station to the source.

390 For event A, based on Fig. 8, the dominance of pure mineral particles is prominent (values greater than 0.8) at all stations, except Antikythera station. This significant transport of pure dust layers, starting from different sources over the Saharan region (Fig. 2a), is reflected on the DOD-to-AOD ratios over a large part of the Eastern Mediterranean and Middle East.

A different situation is presented for event B, where DOD-to-AOD ratio seems to decrease for increasing distance from the source. Specifically, over Bucharest (Magurele\_Inoe), the DOD-to-AOD ratio is  $\sim 0.45$ , almost half that of the first station (Ben\_Salem). Over Magurele\_Inoe, the higher SSA at 440 nm (Fig. 5b), which weakens the characteristic spectral signature of dust, the nearly equal contribution of finer and coarser particles in SD (Fig. 7b) and the lower ASY values (Fig. 4b), highlight the coexistence of coarser dust with finer urban or biomass burning particles. During event B, the extent of the dust transport from the western part of the Sahara affects the whole Mediterranean basin, while over Balkan countries, dust layers seem to be mixed with those arriving from the regions encompassing the Black Sea and overpassing industrialized European cities (e.g.,



400 Milan, Munich, see Fig. 2d).

The smallest contribution of pure dust to the aerosol mixture is recorded during event C (values < 0.6). According to the backward trajectories (Fig. 2e,f), the aerosol layers originated from the Arabian Peninsula, could be affected by both dust particles (e.g., desert regions) and industrial/urban aerosol layers. Event D extends across the entire Mediterranean Basin, with the AERONET stations located on the western part to be affected mainly by layers originating from both the western and central  
405 part of North Africa. Toward the east, the contribution of trajectories originating within the Arabian Peninsula and a large part of Egypt, including the Libyan Desert, is also significant (Fig. 2g,h). According to the DOD-to-AOD ratios, it appears that in apart from the stations operating in urban environments, such as Rome and Athens, all the other stations are characterized by a prominent presence of dust particles (values mainly over  $\sim 0.7$ ). The smaller DOD-to-AOD ratios in combination with the higher contribution of coarse mode (Fig. 7d) and the high ASY values (Fig. 4d) possibly indicate the coexistence of coarse sea  
410 salt particles in the dust layers. This conclusion is also supported by the backward trajectories (Figures 2g,h) with a discernible impact of layers arriving over the western coasts of North Africa from the Atlantic Ocean. Nevertheless, except for event A, the other three events are characterized by the simultaneous presence of dust alongside other fine or coarse-mode particles. Furthermore, even in the case of mineral particles, it is important to consider that their origin plays a critical role in their spectral properties due to the varying mineralogy of dust (Di Biagio et al., 2019).

### 415 4.3 Cyprus: A regional case study

Cyprus was affected by three out of the four selected dust events (A, C, and D), making it possible to utilize ground-based observations on the island to compare the dust events (see Sec.2). Fig. 9 compares dust concentrations over  $\pm 5$  days from the peak of each event at the station (defined by the AERONET observations), highlighting differences in intensity and duration among the events. As seen from this figure whilst event A exhibits higher dust concentrations, event C shows a lower but more  
420 consistent concentration over a longer period. The few observations during event D exhibit similar concentrations with event A before the peak date. The second part of the event (arriving from Middle East) is seen 4 days following the peak day with significant concentrations. Similar trends are seen in the concentration of dominant elements during dust events, i.e., Fe, Al, and Ca, whereas there is no clear trend for Mg, as shown in Fig. 10. It is worth mentioning that, despite the overall lower dust loading during event C, the relative elemental abundance at comparable levels as in event A.

425 The average absorption coefficient calculated by the aethelometers at Agia Marina Xyliatou (see Sec. 2) during events A, C, and D are compared in Fig. 11. When comparing the three events (events A, C, and D), event C exhibits the highest absorption ( $\sim 50\%$  across the entire spectral range, suggesting a greater concentration of absorbing aerosols. Events A and D show similar absorption levels,  $\sim 0.6 Mm^{-1}$  at 440 nm, and much lower for the larger wavelengths. These findings are consistent with previous indicators of mixed aerosol conditions during event C (i.e., lower SSA, Assymetry factor, DOD-to-AOD ratio and  
430 higher Angstrom Exponent). This highlights the source region's significant influence on dust's optical properties. In particular, dust transported from the Middle East appears to be mixed with more absorbing aerosols, potentially carrying anthropogenic pollutants. Previous studies (Bimenyimana et al., 2023; Christodoulou et al., 2023) have identified the Middle East as a major

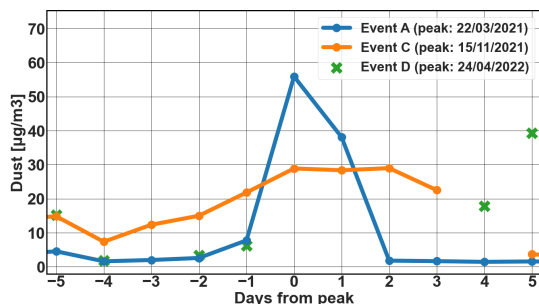


Figure 9. Surface dust concentration measured at CAO-Agia Marina Xyliatou during the events that affected the station.

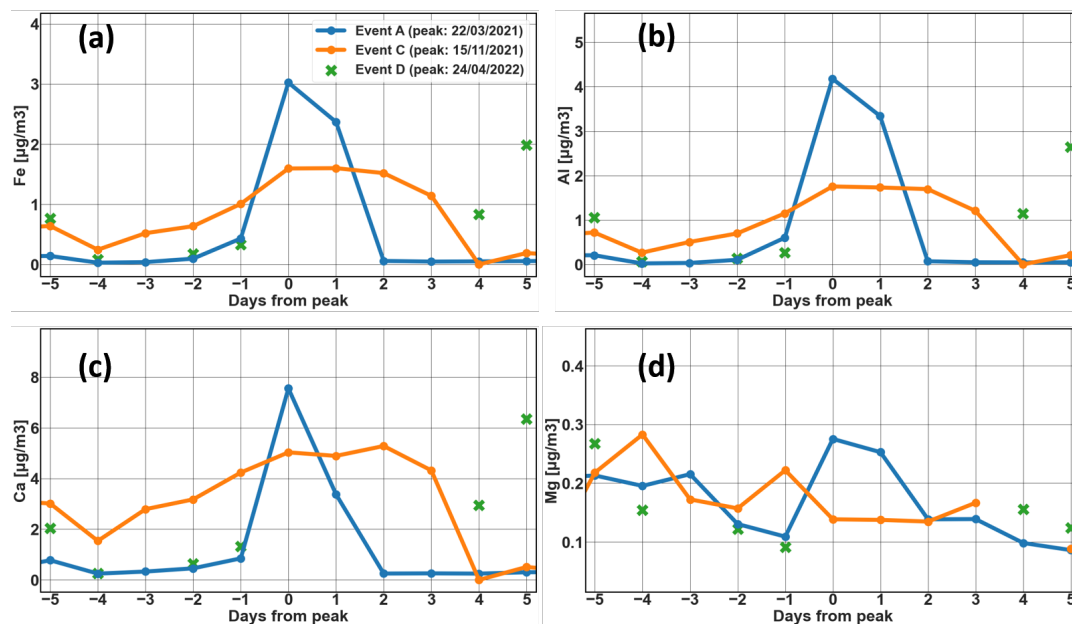
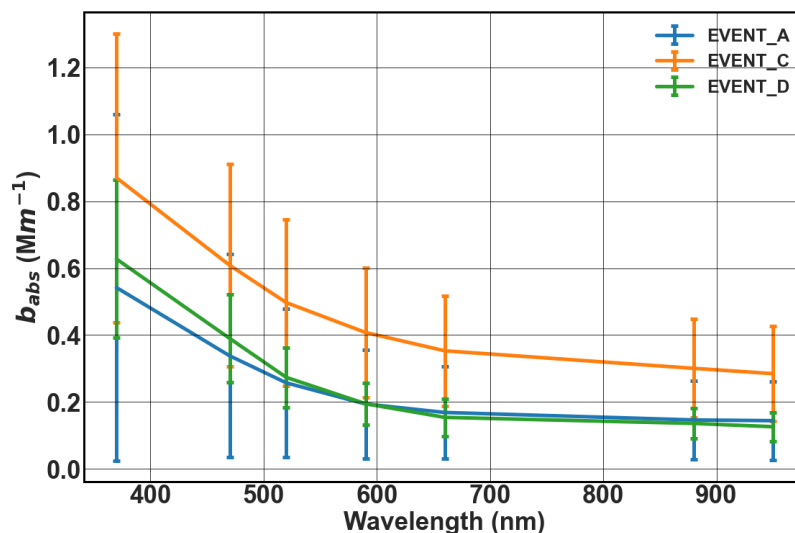


Figure 10. Dominant element ground concentrations (Fe (a), Al (b), Ca (c), and Mg (d)) as measured at CAO-Agia Marina Xyliatou station during events A,C and D.



source of fine particles, including organic aerosols and black carbon, reaching Cyprus, mainly originating from fossil fuel sources.



**Figure 11.** Average absorption coefficient measured during events A (blue line), C (orange line), and D (green line) at CAO Agia Marina Xyliatou station.

#### 435 4.4 Mineralogical simulations

Mineralogical composition of events C and D was simulated using METAL-WRF. The relative abundance of different elements typical for dust at the stations affected during the events is seen in Fig 12. The elemental composition is calculated only at the altitudes with presence of dust. The altitude of dust is derived by applying concentration threshold for iron being  $\geq 1 \text{ gr}/\mu\text{m}^3$ . In this analysis, Agia Marina Xyliatou station is examined for the region of Cyprus to facilitate a direct comparison with the  
 440 in situ results presented herein. The analysis that was done here contributes to a better understanding of: i) the composition differences between events C and D and ii) the variability of composition during the same event across different stations.

As seen also from the observations, the simulated concentrations for event C are, in general, lower than event D. During both events, there is a consistent and intense elemental signature of dust across all stations, with higher concentrations of silica (Si), aluminum (Al) and calcium (Ca), which are enhanced during dust events (Formenti et al., 2008). Within event C, whilst silicon,  
 445 aluminium and calcium are the dominant elements, there is a small variability across stations. Early stations like Weizmann and Sede Boker show higher iron and aluminum concentrations (nearly  $\sim 10\%$  and  $\sim 20\%$  respectively), while stations farther along the dust plume trajectories, like Agia Marina Xyliatou and IMS METU, show decreases in both concentration and elemental diversity. In event D, there is a relatively uniform composition dominated by silicon and aluminum. However, the total concentrations during event D vary significantly, with Lampedusa exhibiting the highest dust loading and Mallorca the  
 450 lowest, suggesting weakening of the plume as it moved westward.



Overall, the relative contribution of the selected elements remains nearly constant (changing by only a few percent) despite large differences in total dust concentration. For example, stations exhibiting concentrations of  $\sim 120 \text{ mg cm}^{-3}$  (Lampedusa, event D) show nearly the same elemental percentage composition as stations with  $\sim 15 \text{ mg cm}^{-3}$  (Mallorca, event D). Therefore, variations in simulated dust composition cannot explain the observed optical differences between stations and events.

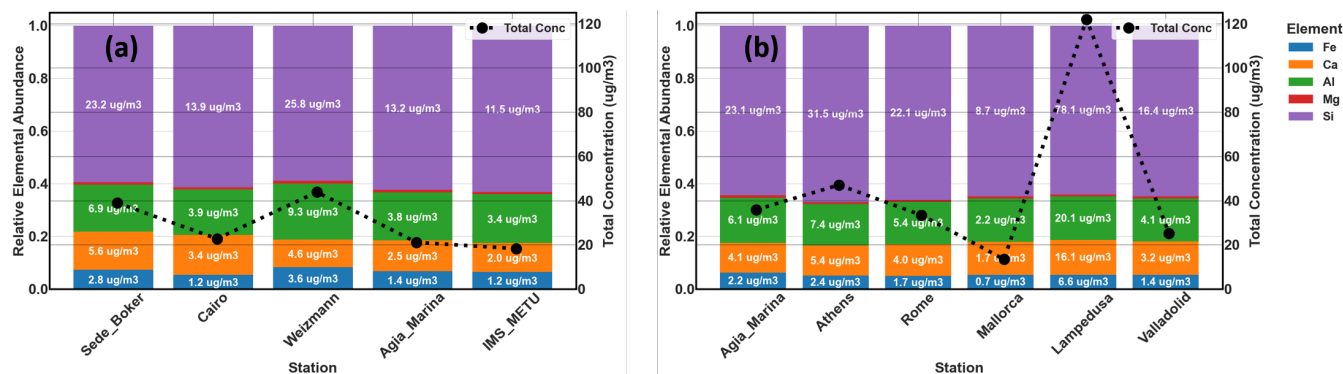


**Figure 12.** Dust-layer averaged relative concentrations of selected elements on AOD peak days during events C (a) and D (b), as simulated by the METAL-WRF model at the affected AERONET stations.

455 To better assess the results of the mineralogical composition from METAL-WRF, the simulated compositions are compared to the in situ observations obtained during Fall Campaign 2021, in Cyprus (Kezoudi et al., 2025), which coincided with event C (see Sec.2).

In Fig. 13, the simulated and observed in situ (ground and UAV-based) dominant dust elements concentrations (Ca, Al, Fe, Si and Mg) are compared during the whole extend of event C. Simulated concentrations were extracted at the same altitudes where  
 460 UAV-based samples were collected and at which there was dust. The ground-based observations (black lines) show significantly higher concentrations (more than double), compared to both the simulated (blue dashed line) and UAV-based measurements (red and green boxes) for calcium and iron. In contrast, an overall good agreement is observed between the UAV-based data and the simulated concentrations for these elements. The average relative deviations are approximately 7% for iron and 9% for calcium, consistent with the findings of Solomos et al. (2023), who also reported good agreement for ground-level iron during  
 465 a 2017 dust event at Agia Marina Xyliatou.

For aluminum and silica, however, the discrepancies between simulated and observed concentrations are substantially larger, with relative deviations ranging between 60% and 80%. Aluminum is notably overestimated by the model at higher altitudes, in contrast to the underestimation reported in the previous study. Magnesium exhibits the largest relative deviations (>200%), likely reflecting its very low absolute concentration levels and associated measurement and modeling uncertainties. Differences between ground-based and elevated-layer observations are generally smaller for aluminum, suggesting a more vertically  
 470 homogeneous distribution of this element.

These statistical comparisons, together with the corresponding z-score values, are summarized in Appendix F, Table F1.

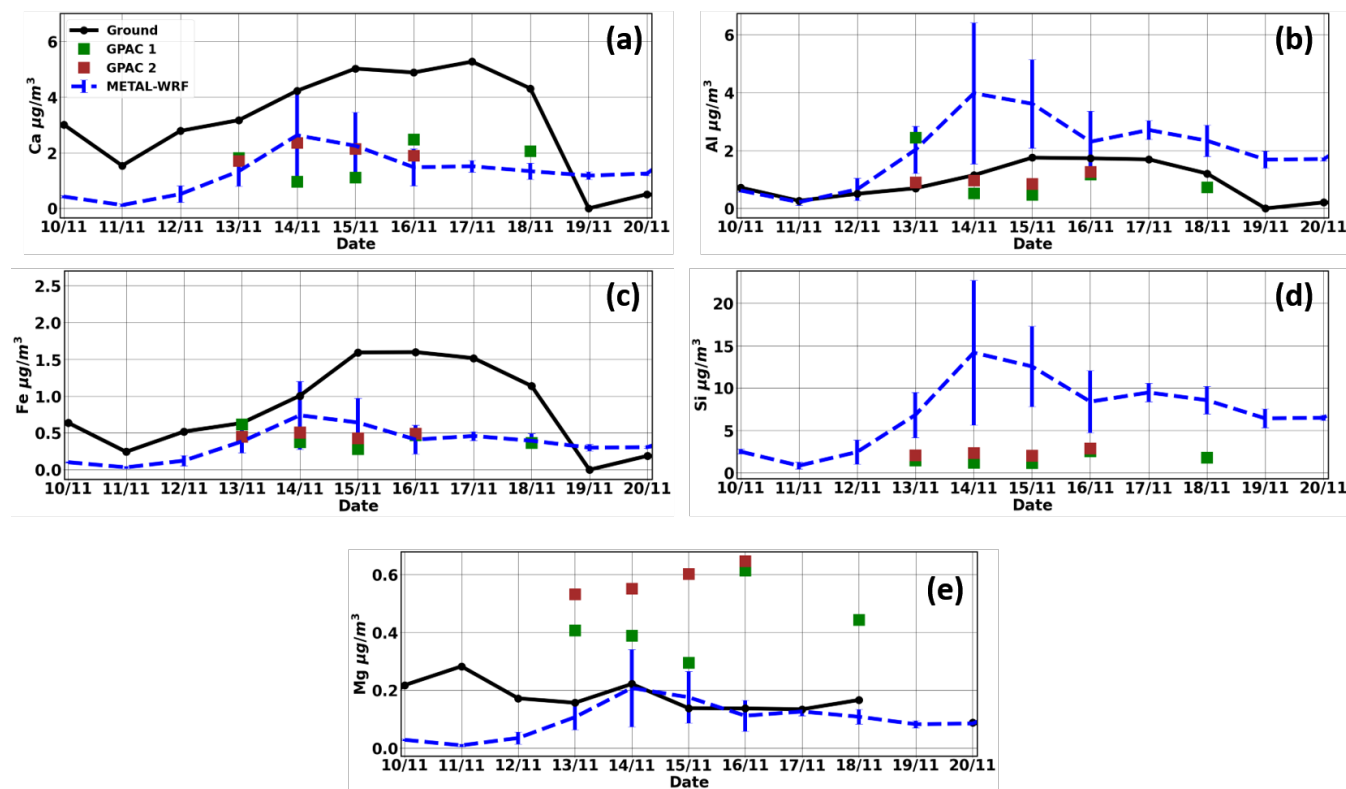


**Figure 13.** Dominant element concentrations (Ca (a), Al (b), Fe (c), Si (d), and Mg (e)) during event C. Solid black lines represent the ground-based observations (no available ground-based measurements for Si). UAV-based observations are represented as boxes at different altitudes for each day: on 11/13, GPAC-1 at 0.1–0.4 km and GPAC-2 1.2–1.8 km a.g.l.; on 11/14 GPAC-1 at 1.1–1.5 and GPAC-2 1.6–2 km a.g.l.; on 11/15 GPAC-1 at 0.5–1.4 km and GPAC-2 1.9–4.4 km a.g.l.; on 11/16 GPAC-1 at 2 km, and GPAC-2 2.2–2.7 km a.g.l.; and on 11/18 GPAC-1 at 0.9–2.8 km a.g.l.. Dashed lines show METAL-WRF simulations of elemental concentration at the altitude ranges covered by the UAV-based observations.

## 5 Conclusions

Dust transport is a frequent phenomenon in the Mediterranean Basin, where it significantly affects regional climate, air quality, 475 ocean biogeochemistry, and human health. However, the dust is often not pure, and the origin, the transport-related processes, and the mixing with local or other transported pollution are difficult to categorize and define. These processes influence the dust’s radiative effects and its environmental impacts, however to-date, they remain poorly represented in many models (Perl- witz et al., 2015; Adebisi and Kok, 2020; Taylor et al., 2015; Mahowald et al., 2025).

This study presents a detailed characterization from AERONET observations of four major desert dust outbreaks in the Mediter- 480 ranean Basin during 2021–2022, with relatively different characteristics. Through this analysis, the spatiotemporal evolution of optical and chemical properties of dust during the events is examined through the synergistic use of ground-based, satellite-



based, and UAV-based observations and models.

The selected events showed substantial differences in terms of optical properties, size distribution, and aerosol composition, depending on their origin and transport pathways. While Saharan events (A, B, D) were predominantly composed of coarse-mode mineral dust, the Middle East event (C) displayed a more complex mixture, with finer, more absorbing particles indicative of anthropogenic origin. This effect was also pronounced at stations where dust had to pass over densely populated or industrial regions, like in the case of Magurele in Romania (event B), highlighting the role of urban pollution and biomass burning in modifying the optical signature of transported dust.

UAV-based in situ measurements and METAL-WRF model outputs provided insights into the mineralogy of the dust events. Both model results and observations indicate that the dust in all examined cases was dominated by silicates and calcium-rich minerals, while iron concentrations remained comparatively low. However, only small variations in mineral contributions were observed between events, suggesting that source-related mineralogical differences were limited during the studied events.

This is the first time, to our knowledge, that chemical composition simulations are evaluated against in situ observations. This exercise was performed by comparing METAL-WRF simulations and UAV-based in situ observations near Agia Marina Xylia-tou, Cyprus, during event C. A good agreement was seen between the two methods for iron and calcium elements (relative deviations  $\leq 40\%$ ), showing the capabilities of the model. On the other hand, the pronounced differences between observations and simulations for aluminum and magnesium, reaching  $\sim 90\%$ , pave the road for further improvements and highlight the importance of such airborne in situ observations for better representation of dust in the models. This finding is particularly relevant given that only few models currently account for dust mineralogical composition, and none are yet operational, highlighting a gap in the full characterization of mineral dust within modeling frameworks. Such targeted comparisons between modeled and observed chemical composition are essential for constraining mineral-specific emissions, transport, and deposition processes. The discrepancies identified for certain elements (e.g., Al and Si) highlight specific pathways for model improvement and demonstrate the added value of airborne campaigns for advancing dust mineralogy modeling. Future dedicated field experiments combining vertical profiling and chemical analysis could improve our understanding and representation of mineral dust in atmospheric models.

Whilst the optical parameters examined in this study (AOD, SSA, AE, ASY, size distribution) exhibited some regional variability between Middle Eastern and Saharan dust, this variability appears to be more strongly linked to changes in the dust-to-total aerosol ratio than to differences in mineral composition. In this context, the dust-to-total aerosol ratio (e.g., MIDAS DOD-to-AOD or AERONET fine mode fraction) is a key parameter controlling the net scattering and absorbing behaviour in the atmospheric column. When interpreted together with SSA and ASY, this ratio provides critical information for radiative transfer calculations, as it not only provides information on the magnitude of solar radiation but also on how it is distributed between direct and diffuse radiation and the angular distribution of scattered light. This information provides essential input for solar energy applications, where an accurate estimation of the diffuse radiation field and sky radiance distribution is required. Therefore, considering both the dust fraction and the optical properties provides more realistic input for radiative transfer models and improves estimates of shortwave radiative forcing and solar energy potential; these parameters have already been applied in the companion study by Kouklaki et al. (2025), which quantifies the shortwave radiative forcing of the four examined events.



Beyond the analysis of the four specific outbreaks, this study demonstrates a comprehensive methodological framework for the in-depth characterization of desert dust events. By combining ground-based sun-photometer observations, satellite-derived dust products, back-trajectory analysis, UAV-based in situ chemical measurements, absorption observations, and mineralogical modeling, we provide a multi-dimensional perspective on dust evolution during transport. This synergistic approach enables the separation of source-related characteristics from transport mixing effects and allows linking the optical properties to both aerosol composition and dust fraction. The methodology presented here can be applied to other dust episodes and regions to improve the characterization of dust events and their radiative impacts.

Overall, this study reinforces the importance of region-specific, event-based analysis to understand the variability of desert dust in a region. Event-specific variability in optical and mineralogical properties highlights the influence of source regions and transport dynamics, emphasizing that dust cannot be treated as a uniform aerosol type. Future work should extend the analysis to a larger number of events over multiple years to improve source-specific characterisation of dust properties and better separate natural dust from anthropogenic contributions. METAL-WRF and other dust models should be further validated with in situ observations across diverse regions to identify biases and enhance predictive capabilities. Datasets from missions like Earth Surface Mineral Dust Source Investigation (EMIT) (Green et al., 2020) can help to resolve current uncertainties in dust mineralogy, and therefore improve the representation of dust in climate models and our ability to assess its environmental and societal impacts.

## Appendix A: ACTRIS/EARLINET aerosol high-power lidars

The EARLINET network (Pappalardo et al., 2014), established in 2000, is the longest-running and the most extensive high-power lidar network in Europe, dedicated to aerosol profile measurements. Several of the EARLINET stations operate nowadays under the aerosol remote sensing component of the Aerosol, Clouds and Trace Gases Research Infrastructure (ACTRIS; Laj et al., 2024), which coordinates and supports their activities. EARLINET network comprises institutions conducting lidar observations, development, and aerosols and clouds research. The network is designed to facilitate scientific collaboration, technological innovation, and fundamental research on aerosol–cloud processes. Currently, 35 active stations contribute to EARLINET, providing extensive spatial coverage across the continent (<https://earlinet.eu/earlinet-map/>, last access: 08 November 2025). Additionally to ACTRIS aerosol remote sensing stations, ACTRIS supports also EARLINET stations not belonging to ACTRIS research infrastructure offering all the services and supports for data processing, data access and provision and in general data curation. ACTRIS also offers support in terms of aerosol lidar system quality assurance and guidance in ACTRIS standard operation procedure compliance.

The geographical distribution of the ACTRIS/EARLINET stations and their routine measurements enable the observation of the three-dimensional temporal evolution of aerosol transport, which can affect vast areas for several days, such as desert dust intrusions (Papanikolaou et al., 2024). In the Mediterranean region, in particular, intense dust episodes are closely monitored by a significant number of ACTRIS/EARLINET stations across the basin, most of which, following ACTRIS requirements, are co-located with AERONET sites. In this study, profiles of aerosol optical properties were used to estimate the height of dust



550 plumes that arrived over the AERONET sites during the four analyzed events. Specifically, profiles of the particle backscatter coefficient and the particle linear depolarization ratio at 532 nm were used to retrieve the dust backscatter coefficient profile, which represents the vertical distribution of dust particles.

Fig. A1 presents an example from a selected ACTRIS/EARLINET station for each of the four events, displaying the particle depolarization ratio profile (blue), and the total aerosol backscatter coefficient profile (yellow), as well as the derived dust  
555 backscatter coefficient profile (orange). In the first event (top left), a measurement from Limassol on 22 March 2021 (Baars and Mamouri, 2024) shows a dust profile extending up to 7 km a.s.l., with two distinct dust layers, the most prominent centered approximately around 2.8 km a.s.l.. During the second event (top right), a measurement from Antikythera on 22 June 2021 (Amiridis, 2025) estimates the dust layer peak at 4 km a.s.l.. For the third (bottom left) and fourth (bottom right) events, both  
560 observed from Limassol, the maximum dust concentration was found at 2.4 km on 15 November 2021 (Baars and Mamouri, 2025a) and at 3.1 km a.s.l. on 24 April 2022 (Baars and Mamouri, 2025b), respectively.

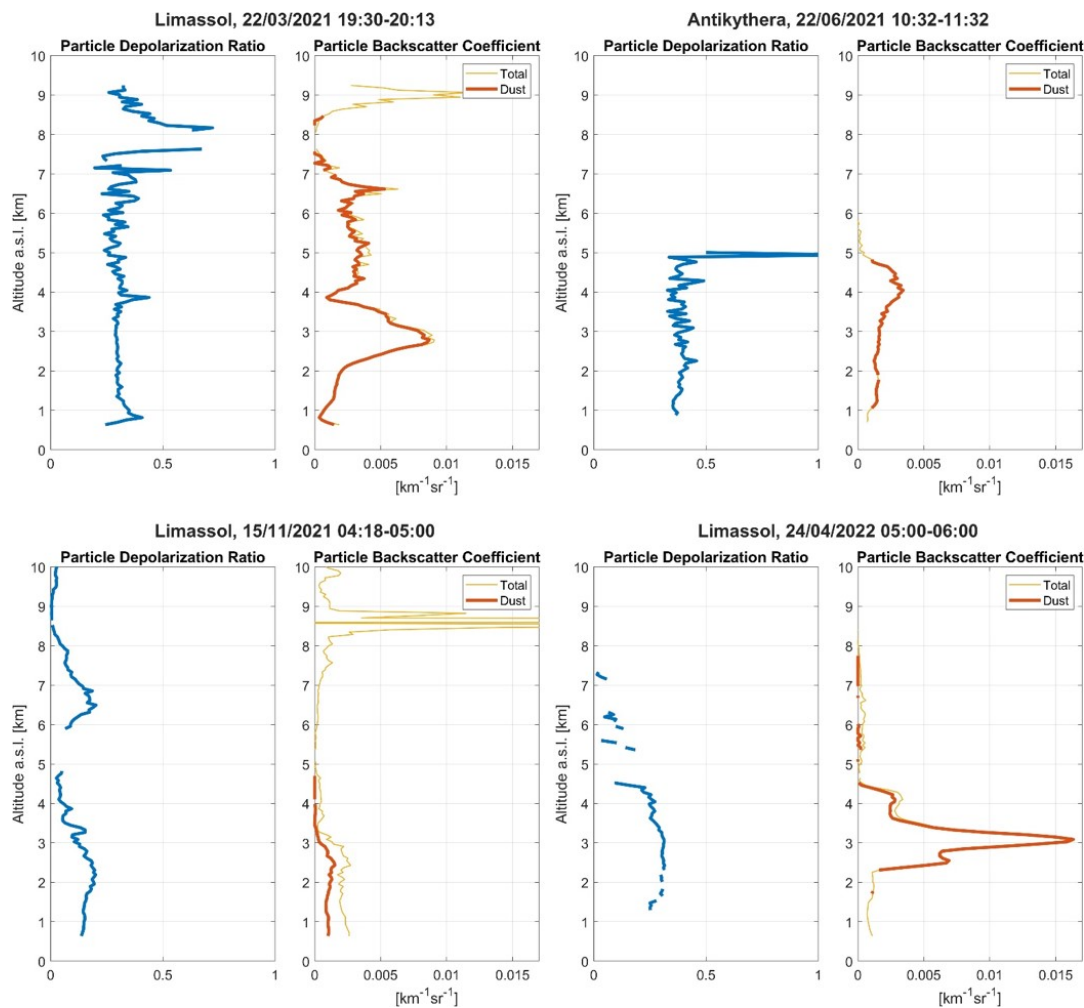


**Figure A1.** The dust component (orange) was separated from the total backscatter coefficient profile (yellow) using the depolarization ratio profile (blue). The lidar measurements were conducted at the following ACTRIS/EARLINET stations: (i) Limassol (34.7 °N, 33.0 °E), Cyprus, on 22/03/2021 during the first event (top left), (ii) Antikythera (35.9 °N, 23.3 °E), Greece, on 22/06/2021 during the second event (top right), (iii) Limassol on 15/11/2021 during the third event (bottom left), and (iv) Limassol on 22/04/2022 during the fourth event (bottom right).

## Appendix B: Atmospheric dust and the LIVAS data record, CALIPSO

Towards investigating the horizontal, vertical, and temporal evolution of the dust events, the four-dimensional atmospheric dust product established by the European Space Agency (ESA) in the framework of the “Lidar climatology of Vertical Aerosol Structure” (LIVAS; Amiridis et al.,2013,2015) project is implemented. More specifically, the LIVAS climate data record is based on the well-established one-step Polarization Lidar PHOTometer Networking (POLIPHON; Tesche et al.,2009) tech-



570  
575

nique, developed within EARLINET activities, applied to optical products provided by CALIOP (Cloud–Aerosol Lidar with Orthogonal Polarization; Hunt et al.,2009) aboard the CALIPSO satellite (Cloud–Aerosol Lidar and Infrared Pathfinder Satellite Observation;Winker et al.,2010), which follows a sun-synchronous polar orbit (Stephens et al., 2018). The final dataset provides quality-assured (Tackett et al., 2018) profiles of the dust backscatter and extinction coefficient (both at 532 nm) and mass concentration, decoupled from the contribution and load of other aerosols, along the CALIPSO orbit path, with 5 km horizontal resolution and the original vertical resolution of CALIOP, for the period June 2006 to August 2023 (Marinou et al., 2017; Proestakis et al., 2024). Figure provides an indicative example, in terms of the CALIPSO overpass (Fig. B1 a), CALIOP profiles of particulate depolarization ratio at 532 nm (Fig. B1 b), the ESA-LIVAS quality-assured profiles of the extinction coefficient for pure dust at 532 nm (Fig. B1 c), and the mean total aerosol (black line) and pure-dust (red line) mean extinction coefficient at 532nm profiles (Fig. B1 d).

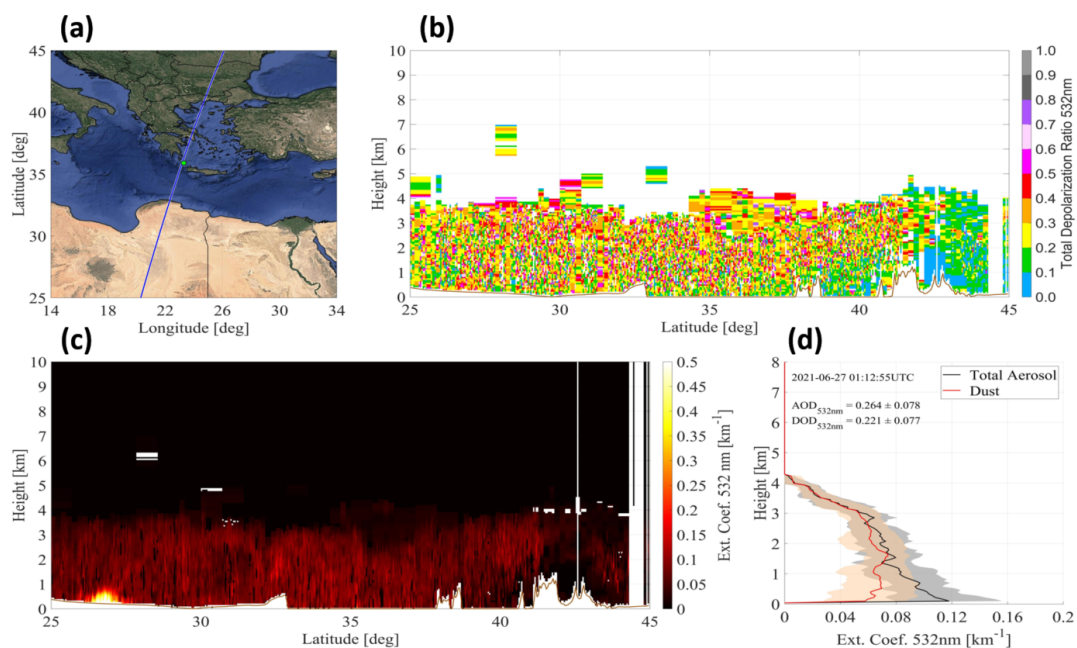


**Figure B1.** CALIPSO nighttime overpass in the proximity of Antikythera station on the 27th of June 2021 and over the broader Eastern Mediterranean region depicting the orbit-track of the satellite ( Map data © 2026 Google Earth) (a), the particulate depolarization ratio at 532 nm profiles (b), the ESA-LIVAS quality-assured pure-dust extinction coefficient at 532 nm profiles (c), and the mean total aerosol (black line) and pure-dust (red line) mean extinction coefficient at 532nm profiles (d).

### Appendix C: MIDAS Maps

Figures C1-C4 illustrate the MODIS derived DOD-to-AOD maps for the four events and the affected stations. As the event peaks on different date at each station, the maps are created for different days. The stations are pinned on the maps with the



580 color of the pins indicating the timeline of the affected stations, with the first station impacted shown in gray and the last in turquoise.

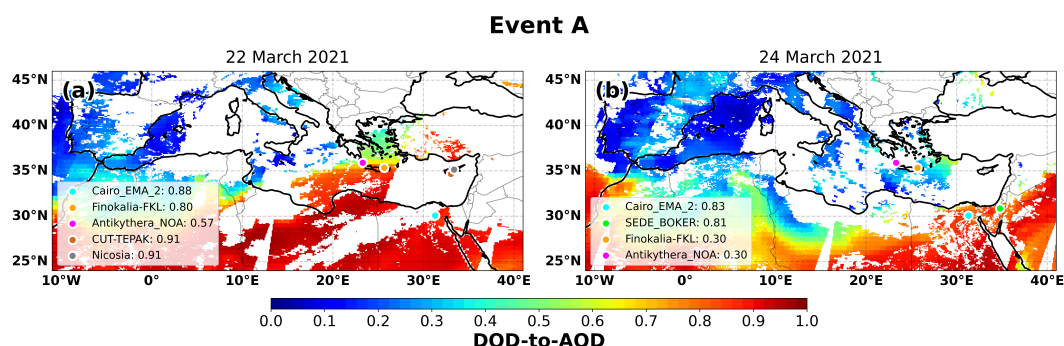


**Figure C1.** DOD-to-AOD ratios (at 550 nm) over the Mediterranean Basin from MIDAS for event A. The days with the available almucantar AERONET retrievals are displayed along with the specific stations (colored circles).

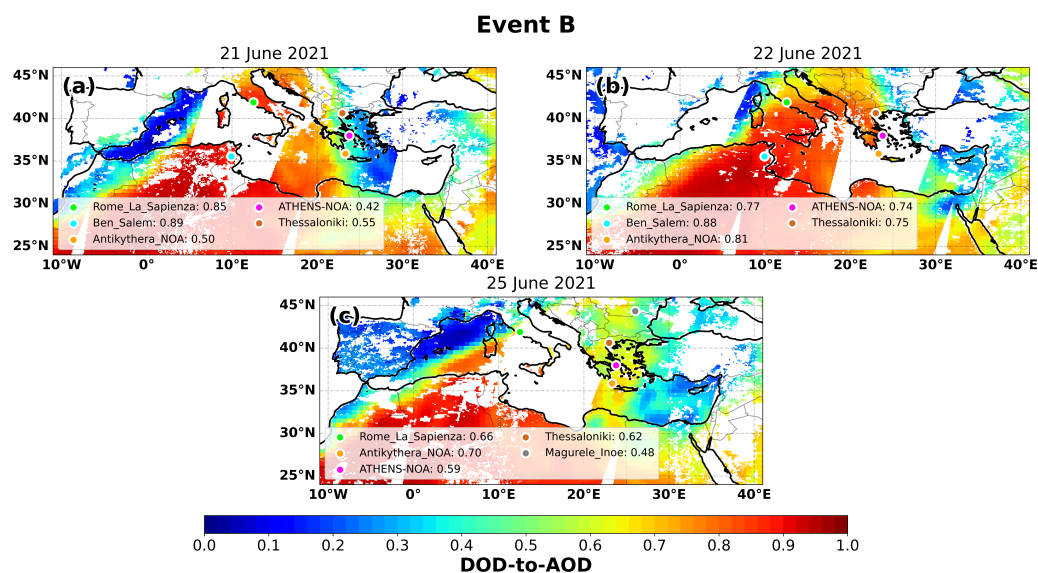


**Figure C2.** DOD-to-AOD ratios (at 550 nm) over the Mediterranean Basin from MIDAS for event B. The days with the available almucantar AERONET retrievals are displayed along with the specific stations (colored circles).

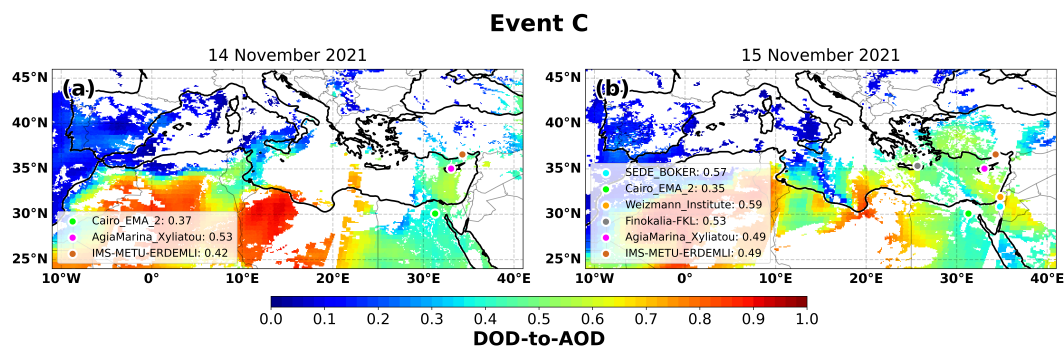


**Figure C3.** DOD-to-AOD ratios (at 550 nm) over the Mediterranean Basin from MIDAS for event C. The days with the available almucantar AERONET retrievals are displayed along with the specific stations (colored circles).

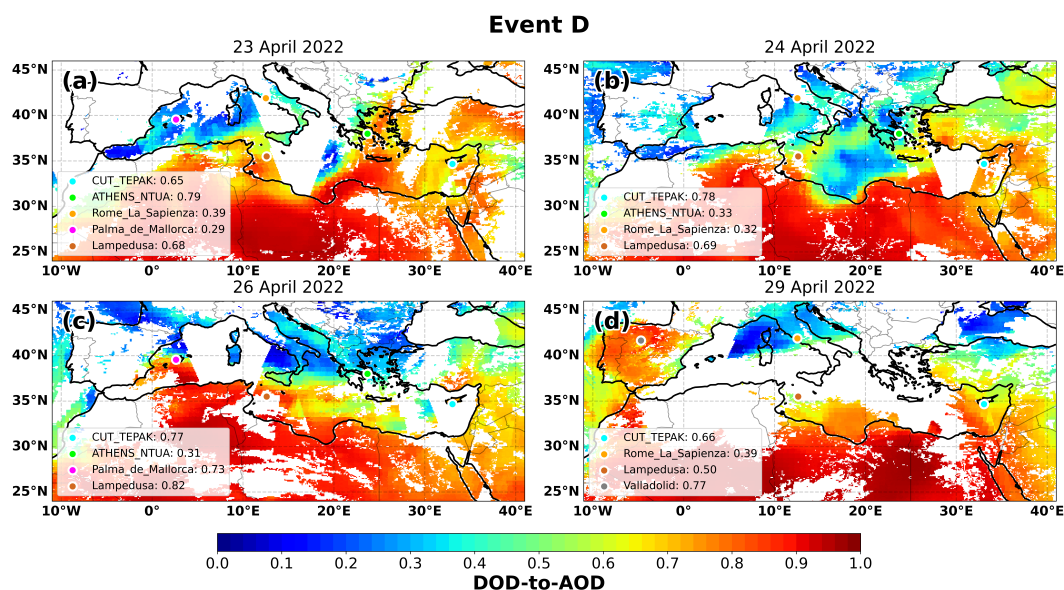


**Figure C4.** DOD-to-AOD ratios (at 550 nm) over the Mediterranean Basin from MIDAS for event D. The days with the available almucantar AERONET retrievals are displayed along with the specific stations (colored circles).



## Appendix D: IASI-MAPIR

The Mineral Aerosol Profiling from Infrared Radiances (MAPIR, Callewaert et al. (2019)) provides vertical profiles of dust aerosol concentration, using remote sensing data from the Infrared Atmospheric Sounding Interferometer (IASI) instrument onboard the Metop satellite series (launched in 2006, 2012 and 2018). Those satellites fly on a sun-synchronous orbit, crossing the equator at about 9h30 and 21h30 local solar time. The IASI observations are done in the thermal infrared (TIR) spectral range, which allows both day and nighttime observations. In addition, the TIR spectral range offers intrinsic specificity to mineral aerosols in comparison to other types and much higher sensitivity to coarse mode particles than to fine mode particles. This means that no post-processing is needed to separate dust from other aerosol types and that the fine particles are mostly absent from the retrieved AOD. The retrieval only works under cloud-free conditions, and the cloud removal is part of the quality check. Figures D1 and D2 present some of the observations during the selected dust events.

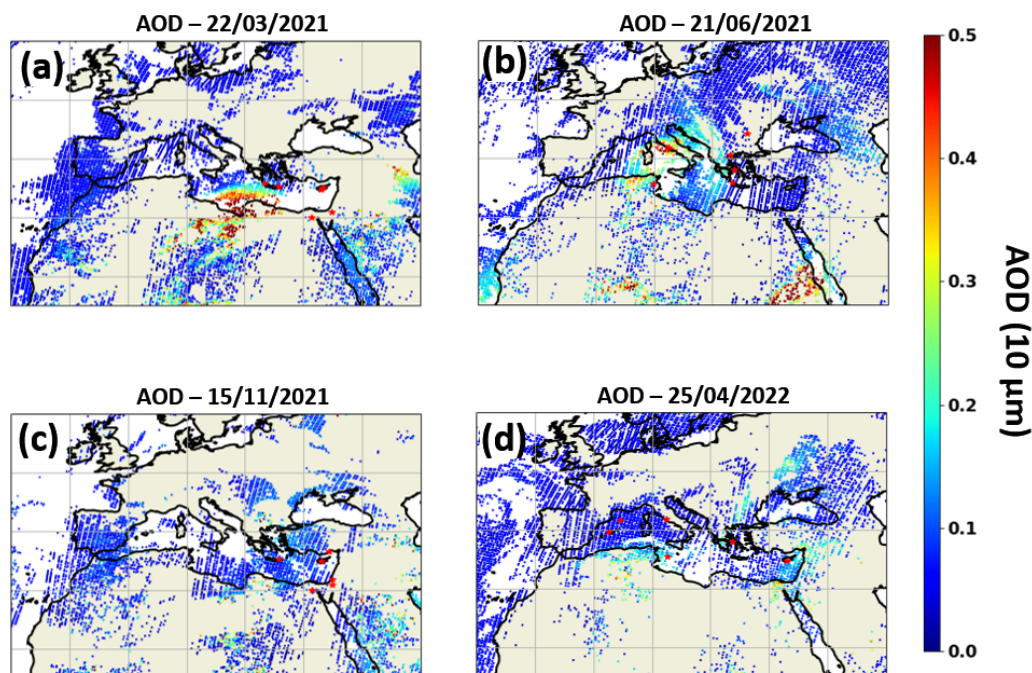


**Figure D1.** Spatial distribution of dust AOD retrieved from IASI-MAPIR during the peak day of the four selected events. Colored pixels represent IASI-derived dust AOD, while blue shading indicates areas with lower dust loading.

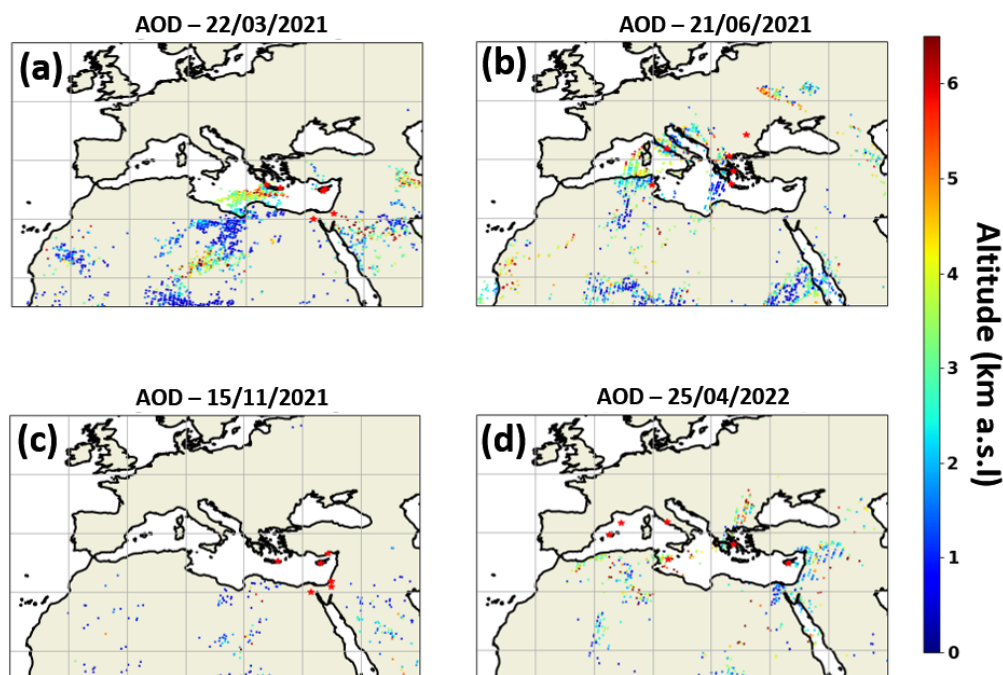


**Figure D2.** Spatial distribution of IASI-MAPIR derived mean dust plume altitude (colored pixels in km a.s.l.), during the four selected dust events.

### Appendix E: AERONET observations

Figures E1 and E2 show the time series of AOD at 500 nm and AE 440-675 nm, respectively, which combined provides insight on the date of arrival and intensity of the dust event at different locations. For event A (see Fig. E1a and E2a) the AOD and AE show a similar evolution between stations, but with different intensity. On March 22, most stations reach an AOD value of approximately 0.8, while over CUT-TEPAK AOD maximum values as high as 1.5 were apparent. Relatively similar AE values were observed in all stations on the days with the highest aerosol loads, with values below 0.5, indicating that a similar aerosol plume with large particles (i.e., dust) was affecting these stations.

During event B (see Fig. E1b and E2b), the AOD and AE evolution was not as uniform as for event A. A first increase in AOD is observed in Bem\_Salem (Tunisian) and Rome\_La\_Sapienza (Central Italy) on June 18, characterized by AE close to 0, which combined are an indication of dust. ATHENS-NOA (Central Greece), Thessaloniki (northern Greece), and Antikythera\_NOA (southern Greece) are affected by the same dust plume 4 days later, with elevated AOD and low AE, between the 21st and the 22nd of June. Magurele\_Inoe (Romania) shows a weaker response to the dust event starting also between the 21st and the 22nd of June and reaching minimum AE and maximum AOD between the 25th and the 26th of June. The highest AOD values are measured in Rome\_La\_Sapienza on June 19 and in Thessaloniki on June 22 with values of 1.2 and 1.5, respectively. Values of



605 AE < 0.2 are observed in Bem\_Salem and Rome\_La\_Sapienza throughout most of the period, with these stations being more affected by the event.

With respect to event C (see Fig. E1c and E2c), the evolution of the AOD and AE properties followed the same temporal pattern in all station observations, similar to event A. A noticeable increase in AOD is observed, especially from the 13th to the 18th of November in Weizmann\_Institute (Israel) and Cairo\_EMA\_2 (Egypt). This increase is also evident in IMS-  
610 METU-ERDEMLI (Turkey), Agia Marina Xyliatou (Cyprus) and Finokalia-FKL (Southern Greece). Except for the high values observed in Cairo\_EMA\_2 at the end of the event, this event shows a lower intensity than the rest of the analyzed events, with AOD values  $\sim 0.4$ . In this case, AE is relatively high and constant in all the stations, with values between 0.5 and 1.6. The highest (around 1.6) and lowest (around 0.5) values are observed in IMS-METU-ERDEMLI (Turkey) and CUT-TEPAK (Cyprus), respectively, with the same minimum observed also at Finokalia-FKL (Greece).

615 Event D (see Fig. E1d and E2d) is characterized by high variability in terms of AERONET observations, possibly attributed to the significant geographical extent of the event, between Eastern and Western Mediterranean. The highest AOD values are observed in Lampedusa (southern Italy) on April 21, when high values are also observed at ATHENS-NOA (Central Greece). During the following days, a decrease is observed in both stations, while on April 23, the AOD increases in CUT-TEPAK (Cyprus) and in Rome\_La\_Sapienza (Central Italy). In addition to Rome\_La\_Sapienza, during the following days, high AOD  
620 values were observed by the rest of the other three stations mentioned, until April 26th, when AOD drops in all these stations except in Lampedusa. On this day, the aerosol plume reaches Palma\_de\_Mallorca (Eastern Spain), and finally on April 29 it arrives in Valladolid (Central Spain). For all the stations, AE reaches values close to 0 on the days when the maximum AOD occurred.

As a next step, the microphysical and optical aerosol properties retrieved by AERONET at the selected station are discussed.  
625 The average of the retrievals that meet the criteria considered (see Sec. 2) are calculated for the day with the highest AOD value at each station for each event. Error bars with standard deviation are plotted for cases where more than one observation are available. For the Middle East and Central Sahara events, it was feasible to retrieve inversions only for some of the stations affected, as not all of the inversions were meeting the criteria.

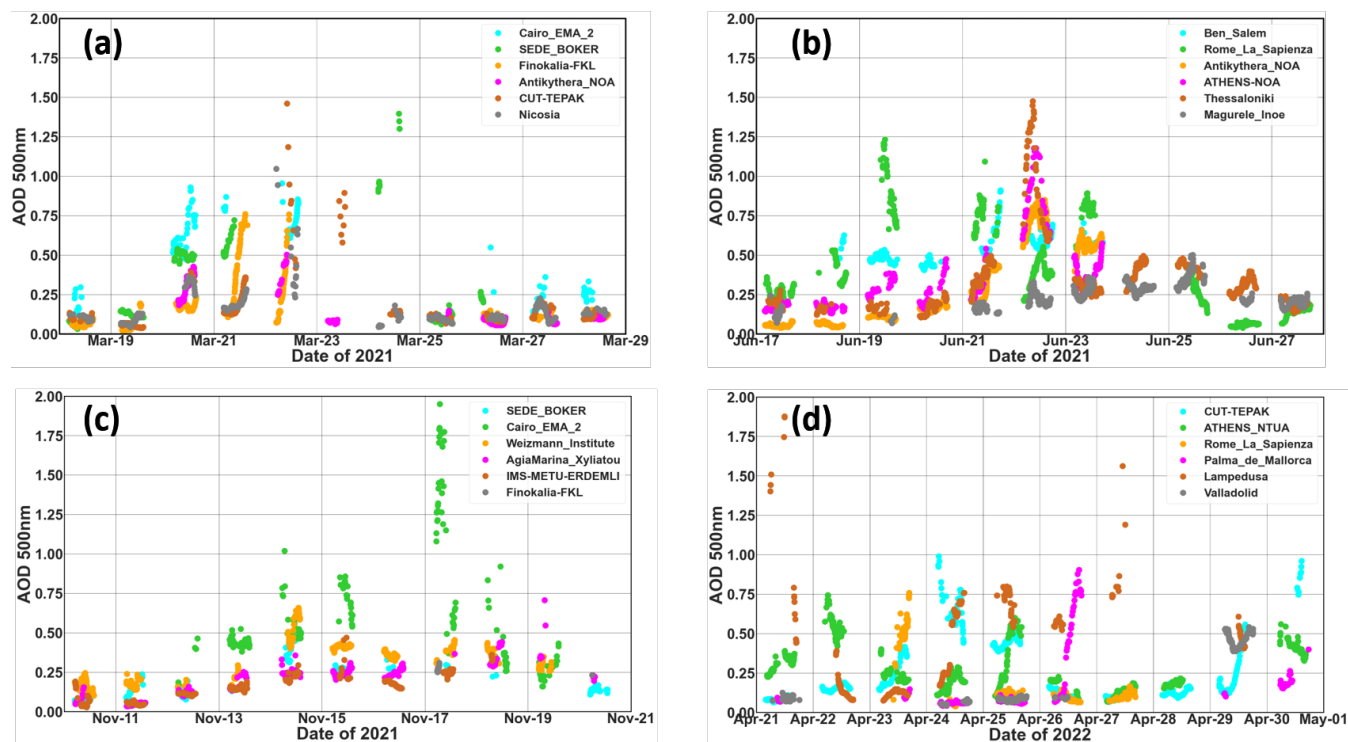


**Figure E1.** Time series AOD at 500 nm at each station for the four events: Event A (A), Event B (B), Event C (C), and Event D (D). Color scheme representing the timeline of affected stations, with the first station in gray and the last in turquoise. The full sequence is: turquoise, green, orange, magenta, brown, and grey.

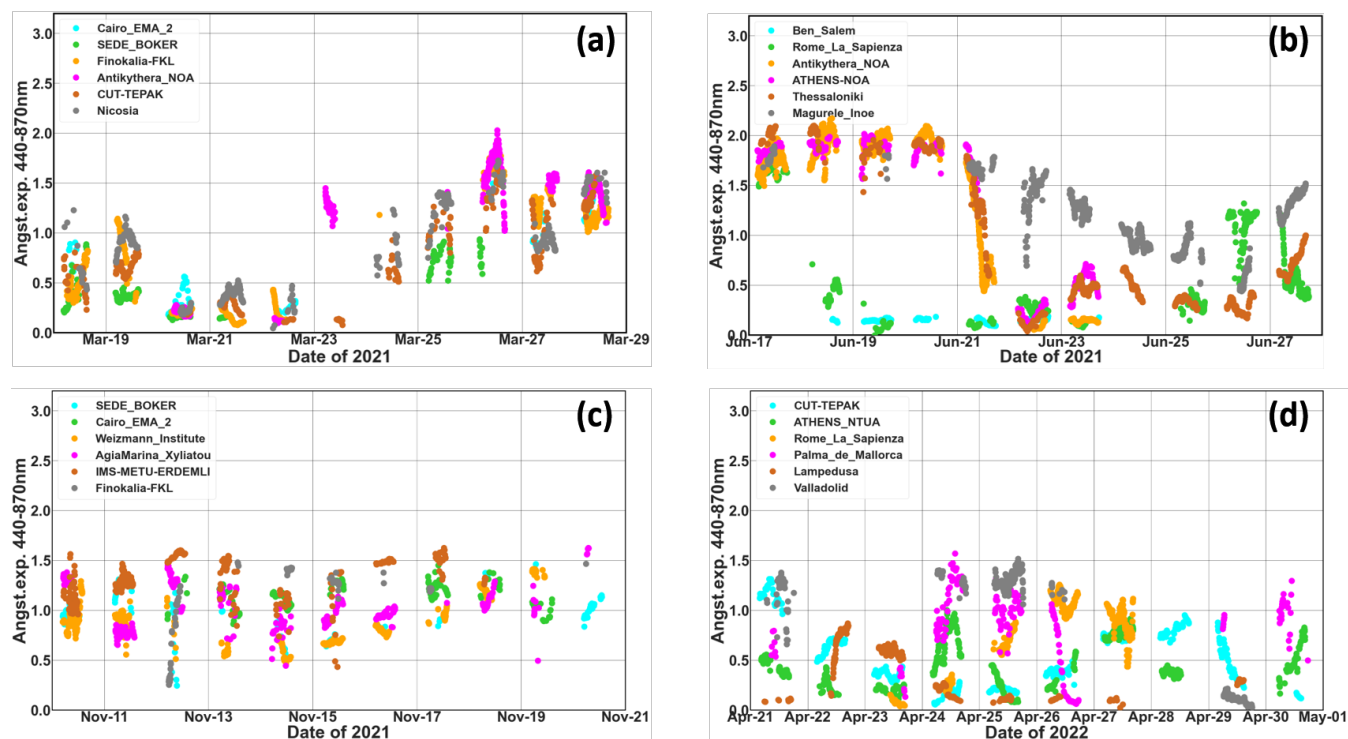


**Figure E2.** Time series of AE 440-675 nm at each station for the four events: Event A (A), Event B (B), Event C (C), and Event D (D). Color scheme representing the timeline of affected stations, with the first station in gray and the last in turquoise. The full sequence is: turquoise, green, orange, magenta, brown, and grey.



## Appendix F: METAL-WRF model evaluation

**Table F1.** Statistical comparison between METAL-WRF simulated and UAV-based (GPAC) observed elemental concentrations during the dust event of 13–18 November 2021. For each sampling date and GPAC ID, the z-score is calculated as  $z = \frac{C_{model} - C_{obs}}{\sigma_{model}}$ , where  $\sigma_{model}$  represents the vertical standard deviation of the simulated concentrations within the corresponding altitude range. The relative difference  $\Delta(\%) = \frac{C_{model} - C_{obs}}{C_{obs}} \times 100$ . Results are shown for Ca, Fe, Mg, Si, and Al. Positive values reflect overestimation by the model, whereas negative values reflect underestimation relative to the UAV observations.

| Date       | GPAC-ID  | Ca      |              | Fe      |              | Mg      |              | Si      |              | Al      |              |
|------------|----------|---------|--------------|---------|--------------|---------|--------------|---------|--------------|---------|--------------|
|            |          | z-score | $\Delta(\%)$ | z-score | $\Delta(\%)$ | z-score | $\Delta(\%)$ | z-score | $\Delta(\%)$ | z-score | $\Delta(\%)$ |
| 11/13/2021 | GPAC_601 | 0.9     | -36.2        | 1.5     | -60.3        | 6.9     | -280.2       | 2.0     | 78.4         | 0.5     | -21.0        |
| 11/13/2021 | GPAC_602 | 0.7     | -27.7        | 0.4     | -17.5        | 9.8     | -396.5       | 1.8     | 69.6         | 1.4     | 55.9         |
| 11/14/2021 | GPAC_603 | 0.2     | 10.1         | 0.5     | 31.1         | 2.6     | -165.1       | 1.4     | 83.6         | 1.2     | 75.9         |
| 11/14/2021 | GPAC_604 | 1.0     | 63.5         | 0.8     | 49.0         | 1.4     | -86.9        | 1.5     | 91.5         | 1.4     | 86.8         |
| 11/15/2021 | GPAC_607 | 0.1     | 5.1          | 0.6     | 33.0         | 4.8     | -242.2       | 2.2     | 83.8         | 1.8     | 76.4         |
| 11/15/2021 | GPAC_608 | 0.9     | 50.8         | 1.1     | 56.2         | 1.3     | -68.0        | 2.4     | 90.6         | 2.1     | 86.9         |
| 11/16/2021 | GPAC_611 | 0.6     | -28.5        | 0.4     | -20.1        | 10.1    | -477.0       | 1.5     | 65.7         | 1.0     | 45.3         |
| 11/16/2021 | GPAC_612 | 1.5     | -67.4        | 0.3     | -14.5        | 9.5     | -447.9       | 1.6     | 69.6         | 1.1     | 49.0         |
| 11/18/2021 | GPAC_701 | 2.5     | -53.8        | 0.3     | 7.7          | 13.1    | -308.3       | 4.1     | 79.0         | 3.0     | 69.0         |

630 *Data availability.* The AERONET products are publicly available at the AERONET website (<https://aeronet.gsfc.nasa.gov/>, last access: 27 February 2026). The IASI-MAPIR dust AOD and mean layer height are available at <https://cds.climate.copernicus.eu/datasets/satellite-aerosol-properties?tab=download>, last access 27 February 2026. The MIDAS dataset is available at <https://doi.org/10.5281/zenodo.4244106> upon request. The CALIPSO lidar level 1B and level 2 data products are publicly available from the Atmospheric Science Data Center at NASA Langley Research Center (<https://earthdata.nasa.gov/eosdis/daacs/asdc>, Earthdata). The LIVAS pure-dust database is available upon personal communication with Emmanouil Proestakis ([proestakis@noa.gr](mailto:proestakis@noa.gr)) and/or Vassilis Amiridis ([vamoir@noa.gr](mailto:vamoir@noa.gr)). The LIVAS L2 pure-dust total, fine-mode, and coarse-mode dataset is available at <https://doi.org/10.5281/zenodo.10389741> (Proestakis, 2023). Three-dimensional METAL-WRF mineralogical simulations are available at <https://doi.org/10.5281/zenodo.20179898> (Spyrou et al.). Ground-based observations from Agia Marina Cyprus and UAV-based mineralogical data are available at <https://doi.org/10.5281/zenodo.20179588> and <https://doi.org/10.5281/zenodo.20179843> (Pikridas and Papetta, 2026; Papetta, 2026)

640 *Author contributions.* Conceptualization, IF and SS within the framework of the HARMONIA COST Action, with contributions from all authors; methodology, all authors; formal analysis, all authors; METAL-WRF simulations, SS and CS; MODIS data analysis, AM and AG; EARLINET data provision and analysis, MM; IASI-MAPIR data analysis, SV; LIVAS-CALIPSO data analysis, EP; Cyprus observational



data acquisition, AP, MK, FM, MP and JS; LIVAS data provision, EP; original draft preparation, AP and CH; writing, review and editing, all authors; All authors have read and agreed to the published version of the manuscript.

645 *Competing interests.* SK is a member of the editorial board of ACP.

*Acknowledgements.* This study is based on the work from COST Action HARMONIA (CA21119), supported by COST (European Cooperation in Science and Technology). The authors would like to sincerely thank Konrad Kandler for performing the SEM analysis of the samples collected during the Fall Campaign in Cyprus. This work was supported by the Ministerio de Ciencia e Innovacion (MICINN), with the grant no. PID2021-127588OB-I00. This work is part of the project TED2021-131211B-I00375 funded by MCIN/AEI/10.13039/501100011033 and European Union, “NextGenerationEU”/PRTR. The authors acknowledge the support from the Spanish Ministry for Science and Innovation for ACTRIS ERIC and from SNF Switzerland for the ACTRIS-CH project. E. PProestakis acknowledges support from the Hellenic Foundation for Research and Innovation (H.F.R.I.) under the “4th Call for H.F.R.I. Research Projects to support Post-Doctoral Researchers” under the project "Earth Observation for Mediterranean Sea biogeochemistry - Dust Soluble Iron Fertilization" (Project Number: 29034). D.Kouklaki would like to acknowledge the PANGEA4CalVal project (Grant Agreement 101079201) funded by the European Union. A. Papetta acknowledges the EMME-CARE project for supporting this work under the European Union’s Horizon 2020 Research and Innovation Programme (Grant Agreement No. 856612). GC would like to acknowledge the EXCELSIOR: ERATOSTHENES: Excellence Research Centre for Earth Surveillance and Space-Based Monitoring of the Environment H2020 Widespread Teaming project (<http://www.excelsior2020.eu/>, accessed on 13 March 2023). The EXCELSIOR 535 project has received funding from the European Union’s Horizon 2020 Research and Innovation Programme under Grant Agreement No 857510, from the Government of the Republic of Cyprus through the Directorate General for the European Programmes, Coordination and Development and the Cyprus University of Technology and ATARRI: This project has received funding from the European Union’s Horizon Europe Twinning Call (HORIZON-WIDERA-2023-ACCESS-02) under the grant agreement No 101160258.



## References

- 665 Adebisi, A., Kok, J. F., Murray, B. J., Ryder, C. L., Stuu, J.-B. W., Kahn, R. A., Knippertz, P., Formenti, P., Mahowald, N. M., Pérez García-Pando, C., Klose, M., Ansmann, A., Samset, B. H., Ito, A., Balkanski, Y., Di Biagio, C., Romanias, M. N., Huang, Y., and Meng, J.: A review of coarse mineral dust in the Earth system, *Aeolian Research*, 60, 100 849, <https://doi.org/10.1016/j.aeolia.2022.100849>, 2023.
- Adebisi, A. A. and Kok, J. F.: Climate models miss most of the coarse dust in the atmosphere, *Science Advances*, 6, eaaz9507, <https://doi.org/10.1126/sciadv.aaz9507>, 2020.
- 670 Al Ameri, I. D. S., Briant, R. M., and Engels, S.: Drought severity and increased dust storm frequency in the Middle East: a case study from the Tigris-Euphrates alluvial plain, central Iraq, *Weather*, 74, 416–426, <https://doi.org/https://doi.org/10.1002/wea.3445>, 2019.
- Amiridis, V.: Aerosol particle backscatter profile at 532nm in Antikythera, Greece at 2021-06-22T10:32 : 2021-06-22T11:32 UTC, ACTRIS Aerosol remote sensing data centre unit (ARES) hosted by CNR IMAA, <https://hdl.handle.net/20.500.12911/1.FK5Z2L55OWAH4CZG>, last access: 21 February 2025, 2025.
- 675 Amiridis, V., Balis, D. S., Kazadzis, S., Bais, A., Giannakaki, E., Papayannis, A., and Zerefos, C.: Four-year aerosol observations with a Raman lidar at Thessaloniki, Greece, in the framework of European Aerosol Research Lidar Network (EARLINET), *Journal of Geophysical Research: Atmospheres*, 110, <https://doi.org/https://doi.org/10.1029/2005JD006190>, 2005.
- Amiridis, V., Wandinger, U., Marinou, E., Giannakaki, E., Tsekeri, A., Basart, S., Kazadzis, S., Gkikas, A., Taylor, M., Baldasano, J., and Ansmann, A.: Optimizing CALIPSO Saharan dust retrievals, *Atmos. Chem. Phys.*, 13, 12 089–12 106, <https://doi.org/10.5194/acp-13-12089-2013>, 2013.
- 680 Amiridis, V., Marinou, E., Tsekeri, A., Wandinger, U., Schwarz, A., Giannakaki, E., Mamouri, R., Kokkalis, P., Biniotoglou, I., Solomos, S., Herekakis, T., Kazadzis, S., Gerasopoulos, E., Proestakis, E., Kottas, M., Balis, D., Papayannis, A., Kontoes, C., Kourtidis, K., Papa-  
giannopoulos, N., Mona, L., Pappalardo, G., Le Rille, O., and Ansmann, A.: LIVAS: a 3-D multi-wavelength aerosol/cloud database based on CALIPSO and EARLINET, *Atmospheric Chemistry and Physics*, 15, 7127–7153, <https://doi.org/10.5194/acp-15-7127-2015>, 2015.
- 685 Andrews, E., Ogren, J. A., Kinne, S., and Samset, B.: Comparison of AOD, AAOD and column single scattering albedo from AERONET retrievals and in situ profiling measurements, *Atmospheric Chemistry and Physics*, 17, 6041–6072, <https://doi.org/10.5194/acp-17-6041-2017>, 2017.
- Aslanoğlu, S. Y., Proestakis, E., Gkikas, A., Güllü, G., and Amiridis, V.: Dust Climatology of Turkey as a Part of the Eastern Mediterranean Basin via 9-Year CALIPSO-Derived Product, *Atmosphere*, 13, 733, <https://doi.org/10.3390/atmos13050733>, 2022.
- 690 Baars, H. and Mamouri, R.: Aerosol particle backscatter profile at 532nm in Limassol, Cyprus at 2021-03-22T19:30 : 2021-03-22T20:13 UTC, ACTRIS Aerosol remote sensing data centre unit (ARES) hosted by CNR IMAA, <https://hdl.handle.net/20.500.12911/1.URGLJGD10RYBPA7W>, last access: 10 February 2026, 2024.
- Baars, H. and Mamouri, R.: Aerosol particle backscatter profile at 532nm in Limassol, Cyprus at 2021-11-15T04:18 : 2021-11-15T05:00 UTC, ACTRIS Aerosol remote sensing data centre unit (ARES) hosted by CNR IMAA, <https://hdl.handle.net/20.500.12911/1.MSW32QGCPZP3UTNF>, last access: 10 February 2026, 2025a.
- 695 Baars, H. and Mamouri, R.: Aerosol particle backscatter profile at 532nm in Limassol, Cyprus at 2022-04-24T05:00 : 2022-04-24T06:00 UTC, ACTRIS Aerosol remote sensing data centre unit (ARES) hosted by CNR IMAA, <https://hdl.handle.net/20.500.12911/1.VVLNWA7YCGK55BMN>, last access: 10 February 2026, 2025b.



- Balis, D. S., Amiridis, V., Nickovic, S., Papayannis, A., and Zerefos, C.: Optical properties of Saharan dust layers as detected by a Raman  
700 lidar at Thessaloniki, Greece, *Geophysical Research Letters*, 31, <https://doi.org/https://doi.org/10.1029/2004GL019881>, 2004.
- Bauer, S. E., Mishchenko, M. I., Laciš, A. A., Zhang, S., Perlwitz, J., and Metzger, S. M.: Do sulfate and nitrate coatings on mineral dust have important effects on radiative properties and climate modeling?, *Journal of Geophysical Research: Atmospheres*, 112, <https://doi.org/https://doi.org/10.1029/2005JD006977>, 2007.
- Bimenyimana, E., Pikridas, M., Oikonomou, K., Iakovides, M., Christodoulou, A., Sciare, J., and Mihalopoulos, N.: Fine  
705 aerosol sources at an urban background site in the Eastern Mediterranean (Nicosia; Cyprus): Insights from offline versus online source apportionment comparison for carbonaceous aerosols, *Science of The Total Environment*, 893, 164741, <https://doi.org/https://doi.org/10.1016/j.scitotenv.2023.164741>, 2023.
- Burgos, M., Mateos, D., Cachorro, V., Toledano, C., and de Frutos, A.: Aerosol properties of mineral dust and its mixtures in a regional background of north-central Iberian Peninsula, *Science of The Total Environment*, 572, 1005–1019,  
710 <https://doi.org/https://doi.org/10.1016/j.scitotenv.2016.08.001>, 2016.
- Cachorro, V. E., Toledano, C., Anton, M., Berjon, A., de Frutos, A., Vilaplana, J. M., Arola, A., and Krotkov, N. A.: Comparison of UV irradiances from Aura/Ozone Monitoring Instrument (OMI) with Brewer measurements at El Arenosillo (Spain) - Part 2: Analysis of site aerosol influence, *Atmos. Chem. Phys.*, 10, 11 867–11 880, <https://doi.org/10.5194/acp-10-11867-2010>, 2010.
- Callewaert, S., Vandenbussche, S., Kumps, N., Kylling, A., Shang, X., Komppula, M., Goloub, P., and Mazière, M. D.: The Mineral  
715 Aerosol Profiling from Infrared Radiances (MAPIR) algorithm: version 4.1 description and evaluation, *Atmos. Meas. Tech.*, p. 26, <https://doi.org/10.5194/amt-12-3673-2019>, 2019.
- Casquero-Vera, J. A., Pérez-Ramírez, D., Lyamani, H., Rejano, F., Casans, A., Titos, G., Olmo, F. J., Dada, L., Hakala, S., Hussein, T., Lehtipalo, K., Paasonen, P., Hyvärinen, A., Pérez, N., Querol, X., Rodríguez, S., Kalivitis, N., González, Y., Alghamdi, M. A., Kerminen, V.-M., Alastuey, A., Petäjä, T., and Alados-Arboledas, L.: Impact of desert dust on new particle formation events and the cloud condensation nuclei budget in dust-influenced areas, *Atmospheric Chemistry and Physics*, 23, 15 795–15 814, <https://doi.org/10.5194/acp-23-15795-2023>,  
720 2023.
- Castellanos, P., Colarco, P., Espinosa, W. R., Guzewich, S. D., Levy, R. C., Miller, R. L., Chin, M., Kahn, R. A., Kempainen, O., Moosmüller, H., Nowotnick, E. P., Rocha-Lima, A., Smith, M. D., Yorks, J. E., and Yu, H.: Mineral dust optical properties for remote sensing and global modeling: A review, *Remote Sensing of Environment*, 303, 113 982, <https://doi.org/https://doi.org/10.1016/j.rse.2023.113982>, 2024.
- 725 Christodoulou, A., Stavroulas, I., Vrekoussis, M., Desservettaz, M., Pikridas, M., Bimenyimana, E., Kushta, J., Ivančić, M., Rigler, M., Goloub, P., Oikonomou, K., Sarda-Estève, R., Savvides, C., Afif, C., Mihalopoulos, N., Sauvage, S., and Sciare, J.: Ambient carbonaceous aerosol levels in Cyprus and the role of pollution transport from the Middle East, *Atmospheric Chemistry and Physics*, 23, 6431–6456, <https://doi.org/10.5194/acp-23-6431-2023>, 2023.
- Cuevas, E., Milford, C., Barreto, A., Bustos, J. J., García, R. D., Marrero, C. L., Prats, N., Bayo, C., Ramos, R., Terradellas, E.,  
730 Suárez, D., Rodríguez, S., de la Rosa, J., Vilches, J., Basart, S., Werner, E., López-Villarrubia, E., Rodríguez-Mireles, S., Pita Toledo, M. L., González, O., Belmonte, J., Puigdemunt, R., Lorenzo, J. A., Oromí, P., and del Campo-Hernández, R.: Desert Dust Outbreak in the Canary Islands (February 2020): Assessment and Impacts, Tech. Rep. GAW Report No. 259, WWRP 2021-1, WMO Global Atmosphere Watch (GAW), State Meteorological Agency (AEMET), World Meteorological Organization (WMO), Madrid, Spain and Geneva, Switzerland, [https://www.aemet.es/documentos/es/conocermas/recursos\\_en\\_linea/publicaciones\\_y\\_estudios/publicaciones/GAW\\_Report\\_No\\_259/GAW\\_Report\\_No\\_259.pdf](https://www.aemet.es/documentos/es/conocermas/recursos_en_linea/publicaciones_y_estudios/publicaciones/GAW_Report_No_259/GAW_Report_No_259.pdf), last accessed: 10 February 2026, 2021.
- 735



- Cuevas-Agulló, E., Barriopedro, D., García, R. D., Alonso-Pérez, S., González-Alemán, J. J., Werner, E., Suárez, D., Bustos, J. J., García-Castrillo, G., García, O., Barreto, A., and Basart, S.: Sharp increase in Saharan dust intrusions over the western Euro-Mediterranean in February–March 2020–2022 and associated atmospheric circulation, *Atmospheric Chemistry and Physics*, 24, 4083–4104, <https://doi.org/10.5194/acp-24-4083-2024>, 2024.
- 740 De Longueville, F., Hountondji, Y.-C., Henry, S., and Ozer, P.: What do we know about effects of desert dust on air quality and human health in West Africa compared to other regions?, *Science of The Total Environment*, 409, 1–8, <https://doi.org/https://doi.org/10.1016/j.scitotenv.2010.09.025>, 2010.
- DeMott, P. J., Sassen, K., Poellot, M. R., Baumgardner, D., Rogers, D. C., Brooks, S. D., Prenni, A. J., and Kreidenweis, S. M.: Correction to African dust aerosols as atmospheric ice nuclei, *Geophysical Research Letters*, 36, <https://doi.org/https://doi.org/10.1029/2009GL037639>,  
745 2009.
- Di Biagio, C., Doussin, J.-F., Cazaunau, M., Pangui, E., Cuesta, J., Sellitto, P., Ródenas, M., and Formenti, P.: Infrared optical signature reveals the source–dependency and along–transport evolution of dust mineralogy as shown by laboratory study, *Scientific Reports*, 13, 13 252, 2023.
- Drinovec, L., Sciare, J., Stavroulas, I., Bezantakos, S., Pikridas, M., Unga, F., Savvides, C., Višić, B., Remškar, M., and Močnik, G.: A  
750 new optical-based technique for real-time measurements of mineral dust concentration in PM<sub>10</sub> using a virtual impactor, *Atmospheric Measurement Techniques*, 13, 3799–3813, <https://doi.org/10.5194/amt-13-3799-2020>, 2020.
- Dubovik, O. and King, M. D.: A flexible inversion algorithm for retrieval of aerosol optical properties from Sun and sky radiance measurements, *Journal of Geophysical Research: Atmospheres*, 105, 20 673–20 696, <https://doi.org/https://doi.org/10.1029/2000JD900282>,  
2000.
- 755 Dubovik, O., Smirnov, A., Holben, B. N., King, M. D., Kaufman, Y. J., Eck, T. F., and Slutsker, I.: Accuracy assessments of aerosol optical properties retrieved from Aerosol Robotic Network (AERONET) Sun and sky radiance measurements, *Journal of Geophysical Research: Atmospheres*, 105, 9791–9806, <https://doi.org/https://doi.org/10.1029/2000JD900040>, 2000.
- Dubovik, O., Holben, B., Eck, T. F., Smirnov, A., Kaufman, Y. J., King, M. D., TanrĀ©, D., and Slutsker, I.: Variability of Absorption and Optical Properties of Key Aerosol Types Observed in Worldwide Locations, *Journal of the Atmospheric Sciences*, 59, 590 – 608,  
760 [https://doi.org/10.1175/1520-0469\(2002\)059<0590:VOAAOP>2.0.CO;2](https://doi.org/10.1175/1520-0469(2002)059<0590:VOAAOP>2.0.CO;2), 2002.
- Ebert, M., Hofmann, H., Jäckel, S., Jaenicke, R., Knippertz, P., Lieke, K., et al.: Size distribution, mass concentration, chemical and mineralogical composition and derived optical parameters of the boundary layer aerosol at Tinfou, Morocco, during SAMUM 2006, *Tellus B: Chemical and Physical Meteorology*, 61, 32–50, 2009.
- Flaounas, E., Kotroni, V., Lagouvardos, K., Kazadzis, S., Gkikas, A., and Hatzianastassiou, N.: Cyclone contribution to dust transport over  
765 the Mediterranean region, *Atmospheric Science Letters*, 16, 473–478, <https://doi.org/https://doi.org/10.1002/asl.584>, 2015.
- Formenti, P., Rajot, J. L., Desboeufs, K., Caquineau, S., Chevaillier, S., Nava, S., Gaudichet, A., Journet, E., Triquet, S., Alfaro, S., Chiari, M., Haywood, J., Coe, H., and Highwood, E.: Regional variability of the composition of mineral dust from western Africa: Results from the AMMA SOP0/DABEX and DODO field campaigns, *Journal of Geophysical Research: Atmospheres*, 113, <https://doi.org/https://doi.org/10.1029/2008JD009903>, 2008.
- 770 Giles, D. M., Holben, B. N., Eck, T. F., Sinyuk, A., Smirnov, A., Slutsker, I., Dickerson, R. R., Thompson, A. M., and Schafer, J. S.: An analysis of AERONET aerosol absorption properties and classifications representative of aerosol source regions, *Journal of Geophysical Research: Atmospheres*, 117, <https://doi.org/https://doi.org/10.1029/2012JD018127>, 2012.



- Giles, D. M., Sinyuk, A., Sorokin, M. G., Schafer, J. S., Smirnov, A., Slutsker, I., Eck, T. F., Holben, B. N., Lewis, J. R., Campbell, J. R., Welton, E. J., Korokin, S. V., and Lyapustin, A. I.: Advancements in the Aerosol Robotic Network (AERONET) Version 3 database – automated near-real-time quality control algorithm with improved cloud screening for Sun photometer aerosol optical depth (AOD) measurements, *Atmospheric Measurement Techniques*, 12, 169–209, <https://doi.org/10.5194/amt-12-169-2019>, 2019.
- 775 Gkikas, A., Hatzianastassiou, N., and Mihalopoulos, N.: Aerosol events in the broader Mediterranean basin based on 7-year (2000 to 2007) MODIS C005 data, *Annales Geophysicae*, 27, 3509–3522, <https://doi.org/10.5194/angeo-27-3509-2009>, 2009.
- Gkikas, A., Hatzianastassiou, N., Mihalopoulos, N., Katsoulis, B. D., and Vardavas, I.: The regime of intense desert dust episodes in the Mediterranean based on contemporary satellite observations and ground measurements, *Atmospheric Chemistry and Physics*, 13, 12 135–12 154, <https://doi.org/10.5194/acp-13-12135-2013>, 2013.
- 780 Gkikas, A., Houssos, E. E., Lolis, C. J., Bartzokas, A., Mihalopoulos, N., and Hatzianastassiou, N.: Atmospheric circulation evolution related to desert-dust episodes over the Mediterranean, *Quarterly Journal of the Royal Meteorological Society*, <https://doi.org/10.1002/qj.2466>, 2014.
- 785 Gkikas, A., Basart, S., Hatzianastassiou, N., Marinou, E., Amiridis, V., Kazadzis, S., Pey, J., Querol, X., Jorba, O., Gassó, S., and Baldasano, J. M.: Mediterranean intense desert dust outbreaks and their vertical structure based on remote sensing data, *Atmospheric Chemistry and Physics*, 16, 8609–8642, <https://doi.org/10.5194/acp-16-8609-2016>, 2016.
- Gkikas, A., Obiso, V., Pérez García-Pando, C., Jorba, O., Hatzianastassiou, N., Vendrell, L., Basart, S., Solomos, S., Gassó, S., and Baldasano, J. M.: Direct radiative effects during intense Mediterranean desert dust outbreaks, *Atmospheric Chemistry and Physics*, 18, 8757–8787, <https://doi.org/10.5194/acp-18-8757-2018>, 2018.
- 790 Gkikas, A., Proestakis, E., Amiridis, V., Kazadzis, S., Di Tomaso, E., Tsekeri, A., Marinou, E., Hatzianastassiou, N., and Pérez García-Pando, C.: ModIs Dust AeroSol (MIDAS): a global fine-resolution dust optical depth data set, *Atmospheric Measurement Techniques*, 14, 309–334, <https://doi.org/10.5194/amt-14-309-2021>, 2021.
- Gkikas, A., Proestakis, E., Amiridis, V., Kazadzis, S., Di Tomaso, E., Marinou, E., Hatzianastassiou, N., Kok, J. F., and García-Pando, C. P.: Quantification of the dust optical depth across spatiotemporal scales with the MIDAS global dataset (2003–2017), *Atmospheric Chemistry and Physics*, 22, 3553–3578, <https://doi.org/10.5194/acp-22-3553-2022>, 2022.
- 795 González-Romero, A., González-Flórez, C., Panta, A., Yus-Díez, J., Reche, C., Córdoba, P., Moreno, N., Alastuey, A., Kandler, K., Klose, M., Baldo, C., Clark, R. N., Shi, Z., Querol, X., and Pérez García-Pando, C.: Variability in sediment particle size, mineralogy, and Fe mode of occurrence across dust-source inland drainage basins: the case of the lower Drâa Valley, Morocco, *Atmospheric Chemistry and Physics*, 23, 15 815–15 834, <https://doi.org/10.5194/acp-23-15815-2023>, 2023.
- 800 Goudie, A. S.: Desert dust and human health disorders, *Environment International*, 63, 101–113, <https://doi.org/https://doi.org/10.1016/j.envint.2013.10.011>, 2014.
- Green, R. O., Mahowald, N., Ung, C., Thompson, D. R., Bator, L., Bennet, M., Bernas, M., Blackway, N., Bradley, C., Cha, J., Clark, P., Clark, R., Cloud, D., Diaz, E., Ben Dor, E., Duren, R., Eastwood, M., Ehlmann, B. L., Fuentes, L., Ginoux, P., Gross, J., He, Y., Kalashnikova, O., Kert, W., Keymeulen, D., Klimesh, M., Ku, D., Kwong-Fu, H., Liggett, E., Li, L., Lundeen, S., Makowski, M. D., Mazer, A., Miller, R. L., Mouroulis, P., Oaida, B., Okin, G. S., Ortega, A., Oyake, A., Nguyen, H., Pace, T., Painter, T. H., Pempejian, J., Pérez García-Pando, C., Pham, T., Phillips, B., Pollock, R., Purcell, R., Realmuto, V., Schoolcraft, J., Sen, A., Shin, S., Shaw, L., Soriano, M., Swayze, G., Thingvold, E., Vaid, A., and Zan, J.: The Earth Surface Mineral Dust Source Investigation: An Earth science imaging spectroscopy mission, in: 2020 IEEE Aerospace Conference, pp. on–line, IEEE, <https://doi.org/10.1109/AERO47225.2020.9172731>, 2020.



- 810 Hatch, C. D., Gierlus, K. M., Schuttelfield, J. D., and Grassian, V. H.: Water adsorption and cloud condensation nuclei activity of calcite and calcite coated with model humic and fulvic acids, *Atmospheric Environment*, 42, 5672–5684, <https://doi.org/https://doi.org/10.1016/j.atmosenv.2008.03.005>, 2008.
- Hess, M., Koepke, P., and Schult, I.: Optical Properties of Aerosols and Clouds: The Software Package OPAC, *Bulletin of the American Meteorological Society*, 79, 831 – 844, [https://doi.org/10.1175/1520-0477\(1998\)079<0831:OPOAAC>2.0.CO;2](https://doi.org/10.1175/1520-0477(1998)079<0831:OPOAAC>2.0.CO;2), 1998.
- 815 Holben, B., Eck, T., Slutsker, I., TanrĀ©, D., Buis, J., Setzer, A., Vermote, E., Reagan, J., Kaufman, Y., Nakajima, T., Lavenu, F., Jankowiak, I., and Smirnov, A.: AERONET: A Federated Instrument Network and Data Archive for Aerosol Characterization, *Remote Sensing of Environment*, 66, 1–16, [https://doi.org/https://doi.org/10.1016/S0034-4257\(98\)00031-5](https://doi.org/https://doi.org/10.1016/S0034-4257(98)00031-5), 1998.
- Holben, B. N., Eck, T. F., Slutsker, I., Smirnov, A., Sinyuk, A., Schafer, J., Giles, D., and Dubovik, O.: AERONET’s Version 2.0 quality assurance criteria, in: *Remote Sensing of the Atmosphere and Clouds, Proc. SPIE 6408*, p. 64080Q, <https://doi.org/10.1117/12.706524>,  
820 2006.
- Hunt, W. H., Winker, D. M., Vaughan, M. A., Powell, K. A., Lucker, P. L., and Weimer, C.: CALIPSO Lidar Description and Performance Assessment, *J. Atmos. Ocean. Technol.*, 26, 1214–1228, <https://doi.org/10.1175/2009JTECHA1223.1>, 2009.
- Ito, A., Adebisi, A. A., Huang, Y., and Kok, J. F.: Less atmospheric radiative heating by dust due to the synergy of coarser size and aspherical shape, *Atmospheric Chemistry and Physics*, 21, 16 869–16 891, <https://doi.org/10.5194/acp-21-16869-2021>, 2021.
- 825 Kalapureddy, M. C. R., Kaskaoutis, D. G., Ernest Raj, P., Devara, P. C. S., Kambezidis, H. D., Kosmopoulos, P. G., and Nastos, P. T.: Identification of aerosol type over the Arabian Sea in the premonsoon season during the Integrated Campaign for Aerosols, Gases and Radiation Budget (ICARB), *Journal of Geophysical Research: Atmospheres*, 114, <https://doi.org/https://doi.org/10.1029/2009JD011826>, 2009.
- Kezoudi, M., Keleshis, C., Antoniou, P., Biskos, G., Bronz, M., Constantinides, C., Desservettaz, M., Gao, R. S., Girdwood, J., Harnetiaux, J., Kandler, K., Leonidou, A., Liu, Y., Lelieveld, J., Marengo, F., Mihalopoulos, N., MoĀnik, G., Neitola, K., Paris, J. D., Pikridas, M., Sarda-Esteve, R., Stopford, C., Unga, F., Vrekoussis, M., and Sciare, J.: The unmanned systems research laboratory (Usrl): A new facility for uav-based atmospheric observations, <https://doi.org/10.3390/atmos12081042>, 2021a.
- 830 Kezoudi, M., Keleshis, C., Antoniou, P., Biskos, G., Bronz, M., Constantinides, C., Desservettaz, M., Gao, R.-S., Girdwood, J., Harnetiaux, J., Kandler, K., Leonidou, A., Liu, Y., Lelieveld, J., Marengo, F., Mihalopoulos, N., MoĀnik, G., Neitola, K., Paris, J.-D., Pikridas, M., Sarda-Esteve, R., Stopford, C., Unga, F., Vrekoussis, M., and Sciare, J.: The Unmanned Systems Research Laboratory (USRL): A New Facility for UAV-Based Atmospheric Observations, *Atmosphere*, 12, <https://doi.org/10.3390/atmos12081042>, 2021b.
- 835 Kezoudi, M., Papetta, A., Kandler, K., Ryder, C. L., Leonidou, A., Keleshis, C., Stopford, C., Thornberry, T., Mamouri, R.-E., Sciare, J., and Marengo, F.: Microphysical and Compositional Differences Between Saharan and Middle Eastern Dust Revealed by UAS Observations, *EGUsphere*, 2025, 1–32, <https://doi.org/10.5194/egusphere-2025-5234>, 2025.
- 840 Kim, D., Chin, M., Yu, H., Eck, T. F., Sinyuk, A., Smirnov, A., and Holben, B. N.: Dust optical properties over North Africa and Arabian Peninsula derived from the AERONET dataset, *Atmospheric Chemistry and Physics*, 11, 10 733–10 741, <https://doi.org/10.5194/acp-11-10733-2011>, 2011.
- Kiriakidis, P., Gkikas, A., Papangelis, G., Christoudias, T., Kushta, J., Proestakis, E., Kampouri, A., Marinou, E., Drakaki, E., Benedetti, A., Rennie, M., Retscher, C., Straume, A. G., Dandoci, A., Sciare, J., and Amiridis, V.: The impact of using assimilated Aeolus wind data on regional WRF-Chem dust simulations, *Atmospheric Chemistry and Physics*, 23, 4391–4417, <https://doi.org/10.5194/acp-23-4391-2023>,  
845 2023.



- Kok, J. F., Storelvmo, T., Karydis, V. A., Adebisi, A. A., Mahowald, N. M., Evan, A. T., He, C., and Leung, D. M.: Mineral dust aerosol impacts on global climate and climate change, *Nature Reviews Earth & Environment*, 4, 71–86, <https://doi.org/10.1038/s43017-022-00379-5>, 2023.
- 850 Korrás-Carraca, M. B., Hatzianastassiou, N., Matsoukas, C., Gkikas, A., and Papadimas, C. D.: The regime of aerosol asymmetry parameter over Europe, the Mediterranean and the Middle East based on MODIS satellite data: evaluation against surface AERONET measurements, *Atmospheric Chemistry and Physics*, 15, 13 113–13 132, <https://doi.org/10.5194/acp-15-13113-2015>, 2015.
- Kosmopoulos, P. G., Kazadzis, S., El-Askary, H., Taylor, M., Gkikas, A., Proestakis, E., Kontoes, C., and El-Khayat, M. M.: Earth-Observation-Based Estimation and Forecasting of Particulate Matter Impact on Solar Energy in Egypt, *Remote Sensing*, 10, 855 <https://doi.org/10.3390/rs10121870>, 2018.
- Kouklaki, E. et al.: Dust radiative effects and impact on energy production over the Mediterranean Basin, in preparation for *Atmospheric Chemistry and Physics*, 2025.
- Laj, P., Myhre, C. L., Riffault, V., Amiridis, V., Fuchs, H., Eleftheriadis, K., Petäjä, T., Salameh, T., Kivekäs, N., Juurola, E., Saponaro, G., Philippin, S., Cornacchia, C., Arboledas, L. A., Baars, H., Claude, A., Mazière, M. D., Dils, B., Dufresne, M., Evangelidou, N., Favez, O., 860 Fiebig, M., Haeffelin, M., Herrmann, H., Höhler, K., Illmann, N., Kreuter, A., Ludewig, E., Marinou, E., Möhler, O., Mona, L., Murberg, L. E., Nicolae, D., Novelli, A., O'Connor, E., Ohneiser, K., Altieri, R. M. P., Picquet-Varrault, B., van Pinxteren, D., Pospichal, B., Putaud, J.-P., Reimann, S., Siomos, N., Stachlewska, I., Tillmann, R., Voudouri, K. A., Wandinger, U., Wiedensohler, A., Apituley, A., Comerón, A., Gysel-Beer, M., Mihalopoulos, N., Nikolova, N., Pietruczuk, A., Sauvage, S., Sciare, J., Skov, H., Svendby, T., Swietlicki, E., Tonev, D., Vaughan, G., Zdimal, V., Baltensperger, U., Doussin, J.-F., Kulmala, M., Pappalardo, G., Sundet, S. S., and Vana, M.: Aerosol, Clouds 865 and Trace Gases Research Infrastructure (ACTRIS): The European Research Infrastructure Supporting Atmospheric Science, *Bulletin of the American Meteorological Society*, 105, E1098 – E1136, <https://doi.org/10.1175/BAMS-D-23-0064.1>, 2024.
- Logothetis, S.-A., Salamalikis, V., Gkikas, A., Kazadzis, S., Amiridis, V., and Kazantzidis, A.: 15-year variability of desert dust optical depth on global and regional scales, *Atmospheric Chemistry and Physics*, 21, 16 499–16 529, <https://doi.org/10.5194/acp-21-16499-2021>, 2021.
- Mahowald, N., Albani, S., Kok, J. F., Engelstaeder, S., Scanza, R., Ward, D. S., and Flanner, M. G.: The size distribution of desert dust 870 aerosols and its impact on the Earth system, *Aeolian Research*, 15, 53–71, <https://doi.org/https://doi.org/10.1016/j.aeolia.2013.09.002>, 2014.
- Mahowald, N. M., Li, L., Vira, J., Prank, M., Hamilton, D. S., Matsui, H., Miller, R. L., Lu, P. L., Akyuz, E., Meidan, D., Hess, P., Lihavainen, H., Wiedinmyer, C., Hand, J., Alaimo, M. G., Alves, C., Alastuey, A., Artaxo, P., Barreto, A., Barraza, F., Becagli, S., Calzolari, G., Chellam, S., Chen, Y., Chuang, P., Cohen, D. D., Colombi, C., Diapouli, E., Dongarra, G., Eleftheriadis, K., Engelbrecht, J., Galy-Lacaux, 875 C., Gaston, C., Gomez, D., González Ramos, Y., Harrison, R. M., Heyes, C., Herut, B., Hopke, P., Hüglin, C., Kanakidou, M., Kertesz, Z., Klimont, Z., Kyllönen, K., Lambert, F., Liu, X., Losno, R., Lucarelli, F., Maenhaut, W., Marticorena, B., Martin, R. V., Mihalopoulos, N., Morera-Gómez, Y., Paytan, A., Prospero, J., Rodríguez, S., Smichowski, P., Varrica, D., Walsh, B., Weagle, C. L., and Zhao, X.: AERO-MAP: a data compilation and modeling approach to understand spatial variability in fine- and coarse-mode aerosol composition, *Atmospheric Chemistry and Physics*, 25, 4665–4702, <https://doi.org/10.5194/acp-25-4665-2025>, 2025.
- 880 Marinou, E., Amiridis, V., Biniotoglou, I., Tsikerdekis, A., Solomos, S., Proestakis, E., Konsta, D., Papagiannopoulos, N., Tsekeri, A., Vlastou, G., Zanis, P., Balis, D., Wandinger, U., and Ansmann, A.: Three-dimensional evolution of Saharan dust transport towards Europe based on a 9-year EARLINET-optimized CALIPSO dataset, *Atmospheric Chemistry and Physics*, 17, 5893–5919, <https://doi.org/10.5194/acp-17-5893-2017>, 2017.



- 885 Marinou, E., Tesche, M., Nenes, A., Ansmann, A., Schrod, J., Mamali, D., Tsekeri, A., Pikridas, M., Baars, H., Engelmann, R., Voudouri, K.-  
A., Solomos, S., Sciare, J., Groß, S., Ewald, F., and Amiridis, V.: Retrieval of ice-nucleating particle concentrations from lidar observations  
and comparison with UAV in situ measurements, *Atmospheric Chemistry and Physics*, 19, 11 315–11 342, <https://doi.org/10.5194/acp-19-11315-2019>, 2019.
- 890 Masoom, A., Kosmopoulos, P., Bansal, A., Gkikas, A., Proestakis, E., Kazadzis, S., and Amiridis, V.: Forecasting dust impact on solar energy  
using remote sensing and modeling techniques, *Solar Energy*, 228, 317–332, [https://doi.org/https://doi.org/10.1016/j.solener.2021.09.033](https://doi.org/10.1016/j.solener.2021.09.033),  
2021.
- Mateos, D., Cachorro, V., Toledano, C., Burgos, M., Bennouna, Y., Torres, B., Fuertes, D., González, R., Guirado, C., Calle, A., and de Frutos,  
A.: Columnar and surface aerosol load over the Iberian Peninsula establishing annual cycles, trends, and relationships in five geographical  
sectors, *Science of The Total Environment*, 518-519, 378–392, [https://doi.org/https://doi.org/10.1016/j.scitotenv.2015.03.002](https://doi.org/10.1016/j.scitotenv.2015.03.002), 2015.
- Middleton, N.: Impacts of sand and dust storms on food production, *Environmental Research: Food Systems*, 1, 022 003,  
895 <https://doi.org/10.1088/2976-601X/ad63ac>, 2024.
- Mona, L., Amiridis, V., Cuevas, E., Gkikas, A., Trippetta, S., Vandenbussche, S., Benedetti, A., Dagsson-Waldhauserova, P., Formenti, P.,  
Haefele, A., Kazadzis, S., Knippertz, P., Laurent, B., Madonna, F., Nickovic, S., Papagiannopoulos, N., Pappalardo, G., García-Pando,  
C. P., Popp, T., Rodríguez, S., Sealy, A., Sugimoto, N., Terradellas, E., Vimic, A. V., Weinzierl, B., and Basart, S.: Observing Mineral  
Dust in Northern Africa, the Middle East, and Europe: Current Capabilities and Challenges ahead for the Development of Dust Services,  
900 *Bulletin of the American Meteorological Society*, 104, E2223 – E2264, <https://doi.org/10.1175/BAMS-D-23-0005.1>, 2023.
- Monteiro, A., Basart, S., Kazadzis, S., Votsis, A., Gkikas, A., Vandenbussche, S., Tobias, A., Gama, C., García-Pando, C. P., Terradellas,  
E., Notas, G., Middleton, N., Kushta, J., Amiridis, V., Lagouvardos, K., Kosmopoulos, P., Kotroni, V., Kanakidou, M., Mihalopoulos,  
N., Kalivitis, N., Dagsson-Waldhauserová, P., El-Askary, H., Sievers, K., Giannaros, T., Mona, L., Hirtl, M., Skomorowski, P., Virtanen,  
T. H., Christoudias, T., Di Mauro, B., Trippetta, S., Kutuzov, S., Meinander, O., and Nickovic, S.: Multi-sectoral impact assessment  
905 of an extreme African dust episode in the Eastern Mediterranean in March 2018, *Science of The Total Environment*, 843, 156 861,  
[https://doi.org/https://doi.org/10.1016/j.scitotenv.2022.156861](https://doi.org/10.1016/j.scitotenv.2022.156861), 2022.
- Nickovic, S., Vukovic, A., Vujadinovic, M., Djurdjevic, V., and Pejanovic, G.: Technical Note: High-resolution mineralogical database of  
dust-productive soils for atmospheric dust modeling, *Atmospheric Chemistry and Physics*, 12, 845–855, <https://doi.org/10.5194/acp-12-845-2012>, 2012.
- 910 Nickovic, S., Vukovic, A., and Vujadinovic, M.: Atmospheric processing of iron carried by mineral dust, *Atmospheric Chemistry and Physics*,  
13, 9169–9181, <https://doi.org/10.5194/acp-13-9169-2013>, 2013.
- Papachristopoulou, K., Fountoulakis, I., Gkikas, A., Kosmopoulos, P. G., Nastos, P. T., Hatzaki, M., and Kazadzis, S.: 15-Year Anal-  
ysis of Direct Effects of Total and Dust Aerosols in Solar Radiation/Energy over the Mediterranean Basin, *Remote Sensing*, 14,  
<https://doi.org/10.3390/rs14071535>, 2022.
- 915 Papanikolaou, C.-A., Papayannis, A., Gidarakou, M., Abdullaev, S. F., Ajtai, N., Baars, H., Balis, D., Bortoli, D., Bravo-Aranda, J. A.,  
Collaud-Coen, M., de Rosa, B., Dionisi, D., Eleftheratos, K., Engelmann, R., Floutsis, A. A., Abril-Gago, J., Goloub, P., Giuliano, G.,  
Gumà-Claramunt, P., Hofer, J., Hu, Q., Komppula, M., Marinou, E., Martucci, G., Mattis, I., Michailidis, K., Muñoz-Porcar, C., Mylonaki,  
M., Mytilinaios, M., Nicolae, D., Rodríguez-Gómez, A., Salgueiro, V., Shang, X., Stachlewska, I. S., Ștefănie, H. I., Szczepanik, D. M.,  
Trickl, T., Vogelmann, H., and Voudouri, K. A.: Large-Scale Network-Based Observations of a Saharan Dust Event across the European  
920 Continent in Spring 2022, *Remote Sensing*, 16, <https://doi.org/10.3390/rs16173350>, 2024.



- Papayannis, A., Amiridis, V., Mona, L., Tsaknakis, G., Balis, D., Bösenberg, J., Chaikovski, A., De Tomasi, F., Grigorov, I., Mattis, I., Mitev, V., Müller, D., Nickovic, S., Pérez, C., Pietruczuk, A., Pisani, G., Ravetta, F., Rizi, V., Sicard, M., Trickl, T., Wiegner, M., Gerding, M., Mamouri, R. E., D'Amico, G., and Pappalardo, G.: Systematic lidar observations of Saharan dust over Europe in the frame of EARLINET (2000–2002), *Journal of Geophysical Research: Atmospheres*, 113, D10 204, <https://doi.org/10.1029/2007JD009028>, 2008.
- 925 Papetta, A.: UAV-based mineralogical composition during Fall Campaign 2021, <https://doi.org/10.5281/zenodo.20179843>, 2026.
- Papi, R., Attarchi, S., Darvishi Bolorani, A., and Neysani Samany, N.: Characterization of Hydrologic Sand and Dust Storm Sources in the Middle East, *Sustainability*, 14, <https://doi.org/10.3390/su142215352>, 2022.
- Pappalardo, G., Amodeo, A., Apituley, A., Comeron, A., Freudenthaler, V., Linné, H., Ansmann, A., Bösenberg, J., D'Amico, G., Mattis, I., Mona, L., Wandinger, U., Amiridis, V., Alados-Arboledas, L., Nicolae, D., and Wiegner, M.: EARLINET: towards an advanced sustainable
- 930 European aerosol lidar network, *Atmospheric Measurement Techniques*, 7, 2389–2409, <https://doi.org/10.5194/amt-7-2389-2014>, 2014.
- Pérez, C., Nickovic, S., Pejanovic, G., Baldasano, J. M., and Özsoy, E.: Interactive dust-radiation modeling: A step to improve weather forecasts, *Journal of Geophysical Research: Atmospheres*, 111, D16 206, <https://doi.org/10.1029/2005JD006717>, 2006.
- Perlwitz, J. P., Pérez García-Pando, C., and Miller, R. L.: Predicting the mineral composition of dust aerosols Part 2: Model evaluation and identification of key processes with observations, *Atmospheric Chemistry and Physics*, 15, 11 629–11 652, [https://doi.org/10.5194/acp-](https://doi.org/10.5194/acp-15-11629-2015)
- 935 15-11629-2015, 2015.
- Pikridas, M. and Papetta, A.: EMEP dataset: Agia Marina Xyliatou, Cyprus, <https://doi.org/10.5281/zenodo.20179588>, 2026.
- Proestakis, E.: A four-dimensional, multiyear, and near-global climate data record of the fine-mode (sub-micrometer in terms of diameter) and coarse-mode (super-micrometer in terms of diameter) components of atmospheric pure-dust, <https://doi.org/10.5281/zenodo.10389741>, 2023.
- 940 Proestakis, E., Amiridis, V., Marinou, E., Georgoulas, A. K., Solomos, S., Kazadzis, S., Chimot, J., Che, H., Alexandri, G., Biniotoglou, I., Daskalopoulou, V., Kourtidis, K. A., de Leeuw, G., and van der A, R. J.: Nine-year spatial and temporal evolution of desert dust aerosols over South and East Asia as revealed by CALIOP, *Atmospheric Chemistry and Physics*, 18, 1337–1362, [https://doi.org/10.5194/acp-18-](https://doi.org/10.5194/acp-18-1337-2018)
- 1337-2018, 2018.
- Proestakis, E., Gkikas, A., Georgiou, T., Kampouri, A., Drakaki, E., Ryder, C. L., Marengo, F., Marinou, E., and Amiridis, V.: A near-
- 945 global multiyear climate data record of the fine-mode and coarse-mode components of atmospheric pure dust, *Atmos. Meas. Tech.*, 17, 3625–3667, <https://doi.org/10.5194/amt-17-3625-2024>, 2024.
- Proestakis, E., Papachristopoulou, K., Georgiou, T., Chatoutsidou, S. E., Lazaridis, M., Gkikas, A., Fountoulakis, I., Tsikoudi, I., Petrakis, M. P., and Amiridis, V.: Atmospheric Dust and Air Quality over large-cities and megacities of the World, *EGUsphere*, 2025, 1–58, <https://doi.org/10.5194/egusphere-2025-1841>, 2025.
- 950 Prospero, J. M.: Long-range transport of mineral dust in the global atmosphere: Impact of African dust on the environment of the southeastern United States, *Proceedings of the National Academy of Sciences*, 96, 3396–3403, <https://doi.org/10.1073/pnas.96.7.3396>, 1999.
- Querol, X., Alastuey, A., Rodriguez, S., Plana, F., Ruiz, C. R., Cots, N., Massagué, G., and Puig, O.: PM10 and PM2.5 source apportionment in the Barcelona Metropolitan area, Catalonia, Spain, *Atmospheric Environment*, 35, 6407–6419, [https://doi.org/https://doi.org/10.1016/S1352-2310\(01\)00361-2](https://doi.org/https://doi.org/10.1016/S1352-2310(01)00361-2), 2001.
- 955 Querol, X., Tobías, A., Pérez, N., Karanasiou, A., Amato, F., Stafoggia, M., Pérez García-Pando, C., Ginoux, P., Forastiere, F., Gumy, S., Mudu, P., and Alastuey, A.: Monitoring the impact of desert dust outbreaks for air quality for health studies, *Environment International*, 130, 104 867, <https://doi.org/https://doi.org/10.1016/j.envint.2019.05.061>, 2019.



- Raptis, I.-P., Kazadzis, S., Amiridis, V., Gkikas, A., Gerasopoulos, E., and Mihalopoulos, N.: A Decade of Aerosol Optical Properties Measurements over Athens, Greece, *Atmosphere*, 11, <https://doi.org/10.3390/atmos11020154>, 2020.
- 960 Rodríguez, S., Riera, R., Fonteneau, A., Alonso-Pérez, S., and López-Darias, J.: African desert dust influences migrations and fisheries of the Atlantic skipjack-tuna, *Atmospheric Environment*, 312, 120 022, <https://doi.org/https://doi.org/10.1016/j.atmosenv.2023.120022>, 2023.
- Rolph, G., Stein, A., and Stunder, B.: Real-time Environmental Applications and Display sYstem: READY, *Environmental Modelling And Software*, 95, 210–228, <https://doi.org/doi.org/10.1016/j.envsoft.2017.06.025>, 2017.
- Ryder, C. L., Bézier, C., Dacre, H. F., Clarkson, R., Amiridis, V., Marinou, E., Proestakis, E., Kipling, Z., Benedetti, A., Parrington, M.,  
965 Rémy, S., and Vaughan, M.: Aircraft engine dust ingestion at global airports, *Natural Hazards and Earth System Sciences*, 24, 2263–2284, <https://doi.org/10.5194/nhess-24-2263-2024>, 2024.
- Sinyuk, A., Holben, B. N., Eck, T. F., Giles, D. M., Slutsker, I., Korokin, S., Schafer, J. S., Smirnov, A., Sorokin, M., and Lyapustin, A.: The AERONET Version 3 aerosol retrieval algorithm, associated uncertainties and comparisons to Version 2, *Atmospheric Measurement Techniques*, 13, 3375–3411, <https://doi.org/10.5194/amt-13-3375-2020>, 2020.
- 970 Solomos, S., Spyrou, C., Barreto, A., Rodríguez, S., González, Y., Neophytou, M. K. A., Mouzourides, P., Bartsotas, N. S., Kalogeri, C., Nickovic, S., Vukovic Vimic, A., Vujadinovic Mandic, M., Pejanovic, G., Cvetkovic, B., Amiridis, V., Sykioti, O., Gkikas, A., and Zerefos, C.: The Development of METAL-WRF Regional Model for the Description of Dust Mineralogy in the Atmosphere, *Atmosphere*, 14, <https://doi.org/10.3390/atmos14111615>, 2023.
- Spyrou, C., Solomos, S., and Papetta, A.: .
- 975 Stein, A. F., Draxler, R. R., Rolph, G. D., Stunder, B. J. B., Cohen, M. D., and Ngan, F.: NOAA HYSPLIT Atmospheric Transport and Dispersion Modeling System, *Bulletin of the American Meteorological Society*, 96, 2059 – 2077, <https://doi.org/10.1175/BAMS-D-14-00110.1>, 2015.
- Stephens, G., Winker, D., Pelon, J., Trepte, C., Vane, D., Yuhas, C., L’Ecuyer, T., and Lebsock, M.: CloudSat and CALIPSO within the A-Train: Ten Years of Actively Observing the Earth System, *B. Am. Meteorol. Soc.*, 99, 569–581, <https://doi.org/10.1175/BAMS-D-16-0324.1>, 2018.
- 980 Tackett, J. L., Winker, D. M., Getzewich, B. J., Vaughan, M. A., Young, S. A., and Kar, J.: CALIPSO lidar level 3 aerosol profile product: version 3 algorithm design, *Atmos. Meas. Tech.*, 11, 4129–4152, <https://doi.org/10.5194/amt-11-4129-2018>, 2018.
- Taylor, M., Kazadzis, S., Amiridis, V., and Kahn, R.: Global aerosol mixtures and their multiyear and seasonal characteristics, *Atmospheric Environment*, 116, 112–129, <https://doi.org/https://doi.org/10.1016/j.atmosenv.2015.06.029>, 2015.
- 985 Teri, M., Gasteiger, J., Heimerl, K., Dollner, M., Schöberl, M., Seibert, P., Tipka, A., Müller, T., Aryasree, S., Kandler, K., and Weinzierl, B.: Pollution affects Arabian and Saharan dust optical properties in the eastern Mediterranean, *Atmospheric Chemistry and Physics*, 25, 6633–6662, <https://doi.org/10.5194/acp-25-6633-2025>, 2025.
- Tesche, M., Ansmann, A., Müller, D., Althausen, D., Engelmann, R., Freudenthaler, V., and Groß, S.: Vertically resolved separation of dust and smoke over Cape Verde using multiwavelength Raman and polarization lidars during Saharan Mineral Dust Experiment 2008, *J. Geophys. Res.-Atmos.*, 114, D13 202, <https://doi.org/10.1029/2009JD011862>, 2009.
- 990 Textor, C., Schulz, M., Guibert, S., Kinne, S., Balkanski, Y., Bauer, S., Bernsten, T., Berglen, T., Boucher, O., Chin, M., Dentener, F., Diehl, T., Easter, R., Feichter, H., Fillmore, D., Ghan, S., Ginoux, P., Gong, S., Grini, A., Hendricks, J., Horowitz, L., Huang, P., Isaksen, I., Iversen, I., Kloster, S., Koch, D., Kirkevåg, A., Kristjansson, J. E., Krol, M., Lauer, A., Lamarque, J. F., Liu, X., Montanaro, V., Myhre, G., Penner, J., Pitari, G., Reddy, S., Seland, Ø., Stier, P., Takemura, T., and Tie, X.: Analysis and quantification of the diversities of aerosol life cycles within AeroCom, *Atmospheric Chemistry and Physics*, 6, 1777–1813, <https://doi.org/10.5194/acp-6-1777-2006>, 2006.

Toledano, C., Cachorro, V. E., Berjon, A., de Frutos, A. M., Sorribas, M., de la Morena, B. A., and Goloub, P.: Aerosol optical depth and Ångström exponent climatology at El Arenosillo AERONET site (Huelva, Spain), *Quarterly Journal of the Royal Meteorological Society*, 133, 795–807, <https://doi.org/https://doi.org/10.1002/qj.54>, 2007.

1000 Valenzuela, A., Olmo, F., Lyamani, H., Antón, M., Titos, G., Cazorla, A., and Alados-Arboledas, L.: Aerosol scattering and absorption Angström exponents as indicators of dust and dust-free days over Granada (Spain), *Atmospheric Research*, 154, 1–13, <https://doi.org/https://doi.org/10.1016/j.atmosres.2014.10.015>, 2015.

1005 Winker, D. M., Pelon, J., Coakley, J. A., Ackerman, S. A., Charlson, R. J., Colarco, P. R., Flamant, P., Fu, Q., Hoff, R. M., Kittaka, C., Kubar, T. L., Le Treut, H., McCormick, M. P., Mégie, G., Poole, L., Powell, K., Trepte, C., Vaughan, M. A., and Wielicki, B. A.: The CALIPSO Mission: A Global 3D View of Aerosols and Clouds, *B. Am. Meteor. Soc.*, 91, 1211–1230, <https://doi.org/10.1175/2010BAMS3009.1>, 2010.

Zeb, B., Alam, K., Khan, R., et al.: Characteristics and optical properties of atmospheric aerosols based on long-term AERONET investigations in an urban environment of Pakistan, *Scientific Reports*, 14, 8548, <https://doi.org/10.1038/s41598-024-58981-0>, 2024.

Zender, C. S., Miller, R. L. L., and Tegen, I.: Quantifying mineral dust mass budgets: Terminology, constraints, and current estimates, *Eos, Transactions American Geophysical Union*, 85, 509–512, <https://doi.org/https://doi.org/10.1029/2004EO480002>, 2004.

1010 Zhang, Z., Li, J., Che, H., Dong, Y., Dubovik, O., Eck, T., Gupta, P., Holben, B., Kim, J., Lind, E., Saud, T., Tripathi, S. N., and Ying, T.: Long-term trends in aerosol properties derived from AERONET measurements, *Atmospheric Chemistry and Physics*, 25, 4617–4637, <https://doi.org/10.5194/acp-25-4617-2025>, 2025.

1015 Zittis, G., Almazroui, M., Alpert, P., Ciais, P., Cramer, W., Dahdal, Y., Fnais, M., Francis, D., Hadjinicolaou, P., Howari, F., Jrrar, A., Kaskaoutis, D. G., Kulmala, M., Lazoglou, G., Mihalopoulos, N., Lin, X., Rudich, Y., Sciare, J., Stenchikov, G., Xoplaki, E., and Lelieveld, J.: Climate Change and Weather Extremes in the Eastern Mediterranean and Middle East, *Reviews of Geophysics*, 60, e2021RG000762, <https://doi.org/https://doi.org/10.1029/2021RG000762>, e2021RG000762 2021RG000762, 2022.